Heliyon 9 (2023) e16579

Contents lists available at ScienceDirect

Heliyon

journal homepage: www.cell.com/heliyon

Research article

Natural convective non-Newtonian nanofluid flow in a wavy-shaped enclosure with a heated elliptic obstacle

Salaika Parvin [a], Nepal Chandra Roy [a,*], Litan Kumar Saha [b]

[a] Department of Mathematics, University of Dhaka, Dhaka 1000, Bangladesh
[b] Department of Applied Mathematics, University of Dhaka, Dhaka 1000, Bangladesh

ARTICLE INFO

Keywords:
Natural convection
Non-Newtonian nanofluid
Magnetohydrodynamic
Wavy-shaped enclosure
Power-law method

ABSTRACT

A numerical investigation has been carried out in a wavy-shaped enclosure with an elliptical inner cylinder to find out the effect of an inclined magnetic field and a non-Newtonian nanofluid on fluid flow and heat transfer. Here, the dynamic viscosity and thermal conductivity of the nanofluid are also taken into account. These properties change with the temperature and nanoparticle volume fraction. The vertical walls of the enclosure are modeled through complex wavy geometries and are kept at a constant cold temperature. The inner elliptical cylinder is deemed to be heated and the horizontal walls are considered adiabatic. Temperature difference between the wavy walls and the hot cylinder leads to natural convective circulation flow inside the enclosure. The dimensionless set of the governing equations and associated boundary conditions are numerically simulated using the COMSOL Multiphysics software, which is based on finite element methods. Numerical analysis has been scrutinized for varying Rayleigh number (Ra), Hartmann number (Ha), magnetic field inclination angle (γ), rotation angle of the inner cylinder (ω), power-law index (n), and nanoparticle volume fraction (ϕ). The findings demonstrate that the solid volumetric concentration of nanoparticles diminishes the fluid movement at greater values of φ. The heat transfer rate decreases for larger nanoparticle volume fractions. The flow strength increases with an increasing Rayleigh number resulting in a best possible heat transfer. A higher Hartmann number diminishes the fluid flow but converse behavior is exhibited for magnetic field inclination angle (γ). The average Nusselt number (Nu_{avg}) values are maximum for $\gamma = 90°$. The power-law index plays a significant role on the heat transfer rate, and results show that the shear-thinning liquid augments the average Nusselt number.

1. Introduction

In the field of heat transfer, researchers are always trying to come up with new ways to increase the efficiency of energy devices by augmenting heat transfer to make energy devices work better. Therefore, they have looked into many physical phenomena to reinforce thermal effectiveness, which increases the efficiency of the heating system [1–3], reduces fuel consumption and results in greater economic savings. For all these reasons, natural convection is preferable to other convection processes, as it is widely used in engineering applications such as cooling operations of electrical equipment, nuclear and chemical reactors, solar technology, heat exchangers and home ventilation. In that case, natural convective heat transfer can be accelerated by modifying the shape of the

* Corresponding author.
E-mail address: nepal@du.ac.bd (N.C. Roy).

https://doi.org/10.1016/j.heliyon.2023.e16579
Received 26 October 2022; Received in revised form 18 May 2023; Accepted 20 May 2023
Available online 1 June 2023

Nomenclature

$\overrightarrow{B}$	vector form of magnetic field $\overrightarrow{B} = (B_x, B_y)$
B_0	strength of magnetic field
c_p	specific heat
d	diameter's of nanoparticles
g→	vector form of gravitational acceleration
g	gravitational acceleration
Ha	Hartmann number
k	thermal conductivity
k_b	Boltzmann constant
l	mean path value
L	Vertical and horizontal length of the outer enclosure
n	power law index
Nu_L	local Nusselt number
Nu_{avg}	average Nusselt number
Pr_T	temperature dependent Prandtl number
Pr	Prandtl number
$\overline{p}$	Pressure
p	dimensionless pressure
R	amplitude ratio (α_1/α_2)
Ra	Rayleigh number
Re	Reynolds number
S	arc length of the inner cylinder
$\overline{\mathrm{T}}$	Temperature
T	dimensionless temperature
$\overline{u}, \overline{v}$	velocity along x axis and y axis
u,v	dimensionless velocity along x axis and y axis
$\overrightarrow{V}$	vector form of velocity
$\overline{x}, \overline{y}$	Cartesian coordinate
x, y	dimensionless Cartesian coordinate

Greek symbols

α	thermal diffusivity
α_1, α_2	sinusoidal function's amplitude
β	thermal expansion coefficient
γ	magnetic field orientation angle
$\dot{\overline{\gamma}}$	second invariant of strain tensor rate
η	angular coordinate
λ	wave length
μ	dynamic viscosity
$\overline{\mu}$	apparent viscosity
ρ	density
σ	electrical conductivity
ψ	stream function
φ	solid volume fraction of nanoparticles

Subscripts

0	cold wal
1	hot wall
H_2O	water
bf	base fluid
nf	nanofluid
np	nanoparticles

geometry design or location of the specified boundary conditions or by boosting the base fluid's thermal conductivity with nanoparticles. Researchers designed tools and techniques for controlling the fluid circulation and heat transfer rate during natural convection. Among these, using different geometries [4–10], existence inside the body [11,12], magnetohydrodynamic (MHD) field insertion [13–15], boundary conditions, several types of Newtonian and non-Newtonian nanoparticles [16–18], etc. have gained a

wide range of importance in engineering applications (see Fig. 27).

Non-Newtonian behavior is common in industrial fluids. Molten solvents and polymers, viscoelastic materials and atomic fluids all have non-Newtonian properties. Understanding the transmission indicators of these fluids is significant since they are increasingly used in a variety of industrial applications. Both Newtonian and non-Newtonian fluids circulation in a closed cavity have been investigated for an extensive variety of uses, such as food processing, fluid movement and polymer engineering. Ozoe and Churchill [19] were the first to investigate the natural convective thermal transportation of non-Newtonian fluids contained in a cavity. Both shear thickening and shear thinning conditions were investigated in a quadrilateral (rectangular) shaped horizontal chamber under natural convection. The critical Rayleigh number was detected as being proportional to the power law index. Li et al. [20] examined free convection on non-Newtonian alumina (Al_2O_3)/water nanofluid contained by a square shaped cavity with a circular cylinder using the LB method. The positive impact of temperature and nanoparticle diameter on viscosity and thermal conductivity were taken into account. Here it is shown that the heat transfer characteristic is directly proportional to the temperature difference and the radius of a circular cylinder, but inversely proportional to the nanoparticle diameter and power law index. Jahanbakhshi et al. [21] scrutinized the condition of the magnetic field of non-Newtonian nanofluid in a complex L-shaped chamber under natural convection. The finite volume approach (FVM) was applied to simulate the governing equations. Results concluded that for shear thinning fluid, the average Nusselt number increased, while for shear thickening fluid, it declined. Ali et al. [22] investigated the influence of pertinent parameters such as the angle of inclination, power-law index and aspect ratio. A U-shaped cavity was crammed with non-Newtonian ferrofluid. The sinusoidal temperature distribution on the bottom wall was also considered. The influence of the power-law index on the heat transfer rate was more significant when the Rayleigh number was larger and the Hartmann number was lower.

Natural convective heat transfer within a complex cavity is often used in the construction of cooling of electronic devices, heat exchangers, double glazed windows, solar collectors, furnaces etc. Complex cavities can be used in many ways that are related to energy system. So it is important to look at how heat moves during natural convection in complex cavities. For instance, an L-shaped enclosure containing Al_2O_3-water nanofluid [23], a C-shaped cavity influenced by a magnetic field [24], a triangular cavity filled with a fluid saturated medium [25,26], a trapezoidal enclosure crammed with nanoparticles [27] and so on. Recently, researchers have taken into account various shapes of enclosures with corrugated walls because this concept is used in solar collectors, building home roofs to make the house cool or hot. Abdulkadhim et al. [28] studied natural convection inside a rectangular enclosure with two sinuous side walls and a wavy inner cylinder. A trapezoidal enclosure with a bottom wavy wall under natural convection crammed with nanofluid-saturated porous medium as considered by Hussein et al. [29].

Nanofluid is a suspension of nano−sized particles in a comparatively low thermally conductive base fluid. Nanotechnology has made significant progress in recent decades. This is mostly due to nanotechnology's widespread use in industrial and engineering products. Nanoparticles have a discrete property in the heat transfer system. Nanoparticles are commonly constructed from metals like silver and copper, metallic oxides like titanium oxide, copper oxide and alumina. Oil, water, and ethylene–glycol mixtures are usually used as primary fluids. Choi [30] was the first to coin the term nanofluid. Many research groups around the world are currently working on nanofluids. Mahmoodi and Hashemi [31] investigated the natural convection of Cu−water nanofluid contained by a C−shaped complex enclosure. Koopaee et al. [32] conducted a paperwork to examine the consequences of MHD natural convective flow within a square enclosure crammed with Al_2O_3−water nanofluid. Free convection within a partially layered porous trapezoidal cavity filled with Ag−water nanofluid was investigated by Abed et al. [33].

The MHD effect has drawn considerable interest from academics in recent decades due to its widespread uses in the cooling of power generators, chemical waste management, nuclear reactors, pollution propagation control [34,35] and other areas. El-Maghlany et al. [36] examined natural convective fluid movement in a magnetically induced enclosure filled with a CuO-water nanofluid. With the aim of solving the non-dimensional equations, the finite volume technique was utilized. Their examination exposed that when the Rayleigh number is very high and the concentration of nanoparticles is raised, heat transfer reaches its maximum with the highest Hartmann number. Rashad et al. [37] numerically studied natural convection and the power of magnetic field and internal heat generation in a porous rectangular enclosure crammed with Cu−water nanofluid. The FEM technique was utilized to obtain the numerical outcome and analyze the effect of several physical parameters. This study revealed that by increasing the range of Hartmann number or the solid particle ratio, the average Nusselt number decays gradually.

This study provides a thorough and in-depth look at how non–Newtonian nanofluids, inclined magnetic field, orientation of inner geometry, variable viscosity and thermal conductivity can enhance natural convective heat transfer in thermal systems. So, the main objective of this study is to analyze the effect of magnetic field flow on natural convective flow in a wavy-shaped enclosure containing a heated elliptic cylinder, also taking into account variable thermal conductivity and viscosity of a non-Newtonian nanofluid. So far as we know, no research has been done on fluid flow and heat transfer in a complex wavy enclosure cavity with an internal elliptic obstacle filled with a non-Newtonian nanofluid with considering variable thermal conductivity and viscosity. Because of this, the current study will add something new to this important scientific field. Complex enclosure shapes that have significant applications in many engineering applications while taking into account several parameters such as Hartmann number, Rayleigh number, magnetic field inclination angle, power-law index and nanoparticle volume fractions along with many physical phenomena such as natural convection, non-Newtonian nanofluids and MHD insertion. With the aim of obtaining the primary findings, all of the aforementioned parameters will be thoroughly investigated in terms of streamline, isotherm and average Nusselt number.

Therefore, the novelty of the present study is the analysis of the combined effects of complex geometry, variable viscosity and thermal conductivity (function of temperature and volume fraction of nanoparticles), and imposed magnetic field in the presence of Al_2O_3-water suspension of a non–Newtonian nanofluid on the natural convection flow and heat transfer. With authors' best knowledge, such kinds of effects have not been addressed yet in the available literature. However, this type of configuration may be found in many engineering applications e.g. solar panels, thermal storage and insulation, power generation systems, geothermal energy, micro-

electromechanical (MEM) devices, cooling mechanisms in electric and electronic devices, lubrications, passive ventilation in buildings, molten metal purification, etc. In some mentioned applications, such as molten metal purification, fusion reactors, and electrical transformers, the thermal-free convection is influenced by a magnetic field and the working fluids can act as non-Newtonian [46,47].

2. Description of physical modeling

Natural convective fluid flow and heat transfer are considered within a geometric framework consisting of an elliptical cylinder at the midpoint of a wavy-shaped enclosure. The physical model with boundary conditions is depicted in Fig. 1. The vertical and horizontal lengths of the outer enclosure are denoted by L. The vertical walls of the cavity are deemed as wavy-shaped and drawn by dint of the following equation:

$$\left.\begin{aligned} G_1(\bar{y}) &= \alpha_1\left[\sin\left(\frac{2\pi\bar{y}}{\lambda}\right) + R\sin\left(\frac{4\pi\bar{y}}{\lambda}\right)\right] \\ G_2(\bar{y}) &= 1 + \alpha_2\left[\sin\left(\frac{2\pi\bar{y}}{\lambda}\right) + R\sin\left(\frac{4\pi\bar{y}}{\lambda}\right)\right] \end{aligned}\right\} \tag{1}$$

Here, in equation (1), α_1 is the sinusoidal function's amplitude, λ defines the wave length, $R = \alpha_1/\alpha_2$ represents the amplitude ratio. In the current problem, the following assumptions have been made:

- The nanofluid used in the analysis is assumed to be non-Newtonian, incompressible and laminar.
- The influence of a uniform inclined magnetic field is taken into consideration.
- The vertical undulating walls of the enclosure are assumed as isothermally cooled and fixed at $\overline{T}_0$.
- The inner elliptic cylinder of the enclosure is considered as heated and kept on $\overline{T}_1$. The outer enclosure's top and bottom walls are considered thermally insulated.
- Fluid flow is caused by a difference in temperature between a hot inner cylinder and cold, wavy vertical walls.
- The empty space between the enclosures is filled with nanofluid. Water is used as the base fluid and alumina (Al_2O_3) is used as the nanoparticle.
- The thermo-physical properties of Al_2O_3−water nanofluid are displayed in Table 1.
- Except for viscosity and thermal conductivity, the physical parameters of nanofluids are considered as constant.
- The Boussinesq approximation estimates the density variation in the body force term of the momentum equation.

For this study, the induced magnetic Reynolds number is very small because of the low values of the considered parameters like nanoparticle concentration and the strength of the magnetic field. Because of this, the Hall effect, Joule heating, induced magnetic field and displacement current are neglected. The effect of radiation is also neglected.

The convective heat transfer is introduced by using a Navier Stokes model for the nanofluid flow. Considering all the above statements, the dimensional governing equations of the nanofluid can be written in vectorial form as follows:

Continuity equation:

$$\nabla \cdot \vec{V} = 0 \tag{2}$$

Momentum equation:

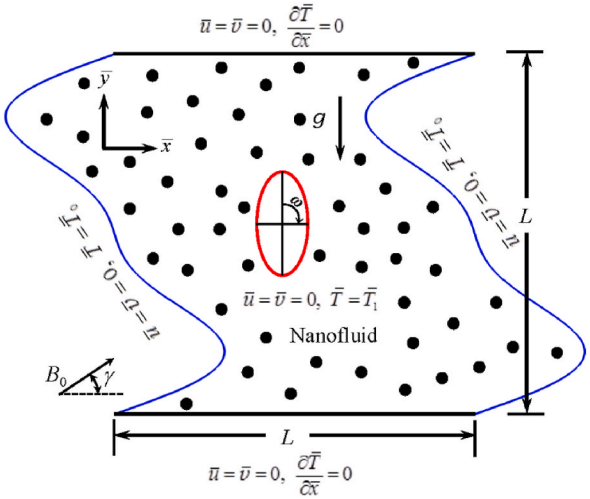

Fig. 1. Representation of the physical diagram.

Table 1
The thermo−physical properties of water (base fluid) and Alumina (Al_2O_3) (solid nanoparticles) [24,39].

Physical Properties	c_p (J/kg K)	ρ (kg/m^3)	k (W/mK)	$\beta \times 10^{-5}$ (1/K)	σ (S/m)	d_{np} (nm)
Water (H_2O)	4179	997.1	0.613	21	0.05	0.384
Alumina (Al_2O_3)	765	3970	25	0.85	10^{-10}	47

$$\rho_{nf}\left(\left(\vec{V}\cdot\nabla\right)\vec{V}\right) = -\nabla\overline{p} + \nabla\cdot\left[\overline{\mu}\left(\nabla\vec{V} + \left(\nabla\vec{V}\right)^{T}\right)\right] + (\rho\beta)_{nf}(\overline{T}-\overline{T}_0)\vec{g} + \sigma_{nf}\left[\vec{V}\times\vec{B}\right]\times\vec{B} \tag{3}$$

Energy equation:

$$(\rho c_p)_{nf}\left(\left(\vec{V}\cdot\nabla\right)\overline{T}\right) = \nabla\cdot(\alpha_{nf}\nabla\overline{T}). \tag{4}$$

In equation (3), $((\vec{V}\cdot\nabla)\vec{V})$ defines the momentum convection and indicates the speed and direction which the fluid is moving, $\nabla\overline{p}$ specifies the pressure gradient, $\overline{\mu}\,(\nabla\vec{V}+(\nabla\vec{V})^{T})$ indicates momentum diffusion, $(\rho\beta)_{nf}(\overline{T}-\overline{T}_0)\vec{g}$ implies the body force acts on nanofluid known as gravitational force, $[\vec{V}\times\vec{B}]\times\vec{B}$ point to the another body force magnetic force. In equation (4), $((\vec{V}\cdot\nabla)\overline{T})$ specifies heat convection and $\nabla\cdot(\alpha_{nf}\nabla\overline{T})$ indicates thermal diffusion of nanofluid.

In the expressions above, T_0, $\overline{T}$, $\vec{V} = \overline{u}\hat{i} + \overline{v}\hat{j}$, $\overline{p}$, $\vec{g}$ are specified the surrounding temperature, nanofluid temperature, velocity vector ($\overline{u}$ the velocity along the bottom wall (along $\overline{x}$ −axis) and $\overline{v}$ the velocity along $\overline{y}$ −axis), pressure and vector form of gravitational acceleration which acts along the negative $\overline{y}$ −axis, respectively. The magnetic field vector $\vec{B}$ which is defined as $\vec{B} = (B_x, B_y)$ where $B_x = B_0\cos\gamma$, $B_y = B_0\sin\gamma$. B_0 denotes the strength of the magnetic field and γ signifies the magnetic field orientation angle. $\overline{\mu}$ is the sign of shear rate dependent viscosity.

The apparent viscosity ($\overline{\mu}$) is a function of shear rate. This relation is expressed by the power law model as follows:

$$\overline{\mu} = \overline{\mu}_{nf}|\overline{\dot{\gamma}}|^{(n-1)} \tag{5}$$

where, $\overline{\mu}_{nf}$ is the effective dynamic viscosity, $\overline{\dot{\gamma}}$ is the second invariant of strain tensor rate and n defines the power law index or flow behavior index. This relation approximately distinguishes the behavior of fluid types. For $n < 1$, the viscosity is shear-thinning or pseudoplastic such as ketchup, nail polish, blood and paint. For $n > 1$, the viscosity is Shear-thickening or dilatant such as corn starch and water (Oobleck) and for $n = 1$, the above equation (5) reduces to a Newtonian viscosity model like water, air, oil, glycerol and alcohol.

For two-dimensional flow the explicit form of $|\overline{\dot{\gamma}}|$ is expressed as,

$$|\overline{\dot{\gamma}}| = \left(2\left(\frac{\partial\overline{u}}{\partial\overline{x}}\right)^2 + 2\left(\frac{\partial\overline{v}}{\partial\overline{y}}\right)^2 + \left(\frac{\partial\overline{u}}{\partial\overline{y}} + \frac{\partial\overline{v}}{\partial\overline{x}}\right)^2\right)^{1/2}$$

The current study considers Abu−Nada [39] and Chon et al. [38] process for calculating temperature and nanoparticle volume fraction dependent viscosity and thermal conductivity of a nanofluid. The approximation of nanofluid's effective thermal conductivity is calculated by Chon et al. [38]:

$$\frac{k_{nf}}{k_{bf}} = 1 + 64.7\varphi^{0.764}\left(\frac{d_{bf}}{d_{np}}\right)^{0.369}\left(\frac{k_{np}}{k_{bf}}\right)^{0.7476}\mathrm{Pr}_T{}^{0.9955}\mathrm{Re}^{1.2321} \tag{6}$$

where, φ signifies the solid volume fraction of nanoparticles of diameter d_{np} with thermal conductivity k_p, d_{bf} is the diameter of pure fluid molecular with thermal conductivity k_{bf}. Pr_T and Re respectively known as the Prandtl and Reynolds number and expressed as,

$$\mathrm{Pr}_T = \frac{\mu_{bf}}{\rho_{bf}\alpha_{bf}}, \mathrm{Re} = \frac{\rho_{bf}k_b\overline{T}}{3\pi\mu_{bf}^2 l_{bf}} \tag{7}$$

ρ_{bf} is the base fluid density, k_b is the Boltzmann constant, 1.3807 × 10^{-23} J/K, l_{bf} is the mean path value of the primary fluid particles specified as 0.17 nm and the temperature dependent base fluid viscosity is expressed as,

$$\mu_{bf} = 2.414\times10^{-5}\times10^{247.8/(\overline{T}-140)} \tag{8}$$

The correlation for the dynamic viscosity of water−based Alumina (Al_2O_3) nanofluid was constructed by Abu−Nada [39] using available data from Nguyen et al. [40]:

$$\begin{aligned}\mu_{nf}(\mathrm{cp}) = &-0.151 - \frac{19.582}{\overline{T}} + 0.794\varphi + \frac{2094.47}{\overline{T}^2} - 0.192\varphi^2 - 8.11\frac{\varphi}{\overline{T}} - \frac{27463.863}{\overline{T}^3}\\ &+0.127\varphi^3 + 1.6011\frac{\varphi^2}{\overline{T}} + 2.1754\frac{\varphi}{\overline{T}^2}\end{aligned} \tag{9}$$

In this current study, equations (6)–(9) are considered for calculating temperature and nanoparticle volume fraction dependent thermal conductivity and viscosity, respectively, of Al_2O_3–water nanofluid.

The viscosity of the pure fluid (water) is considered a function of temperature and the following equation is applied to calculate the water viscosity:

$$\mu_{H_2O}(\text{cp}) = -81.1 + 98.75\ln(\overline{T}) - 45.23\ln(\overline{T}^2) + 9.71\ln(\overline{T}^3) - 0.946\ln(\overline{T}^4) + 0.03\ln(\overline{T}^5) \tag{10}$$

The viscosity equations (9) and (10) are considered in centi poise (cp) and temperature in °C. The comparison between the experimental data of Nguyen et al. [40] and the correlation of Abu−Nada [39], is revealed in Fig. 2(a) and (b), respectively. In this case, the viscosity of Al_2O_3−water nanofluid is calculated by using equation (9). The approximate value of μ_{nf}(cp) is crosschecked to the numerical examination for distinct values of concentration ratio of nanoparticles.

The physical and thermal properties of the nanofluids have been calculated with the following formulas [35]:

The effective dynamic viscosity [41]:	$\mu_{nf} = \frac{\mu_f}{(1-\varphi)^{2.5}}$	(11)
The effective density:	$\rho_{nf} = (1-\varphi)\rho_{bf} + \varphi\rho_{np}$	(12)
The effective thermal diffusivity:	$\alpha_{nf} = k_{nf}/(\rho c_p)_{nf}$	(13)
The effective heat capacitance:	$(\rho c_p)_{nf} = (1-\varphi)(\rho c_p)_{bf} + \varphi(\rho c_p)_{np}$	(14)
The effective thermal expansion coefficient:	$(\rho\beta)_{nf} = (1-\varphi)(\rho\beta)_{bf} + \varphi(\rho\beta)_{np}$	(15)
The effective thermal conductivity [42]:	$k_{nf} = k_{bf}\left[\frac{(k_{np}+2k_{bf}) - 2\varphi(k_{bf}-k_{np})}{(k_{np}+2k_{bf}) + \varphi(k_{bf}-k_{np})}\right]$	(16)
The effective electrical conductivity:	$\frac{\sigma_{nf}}{\sigma_{bf}} = 1 + \frac{3\left(\frac{\sigma_{np}}{\sigma_{bf}} - 1\right)\varphi}{\left(\frac{\sigma_{np}}{\sigma_{bf}} + 2\right) - \left(\frac{\sigma_{np}}{\sigma_{bf}} - 1\right)\varphi}$	(17)

In the above equations (11)–(17), the subscripts '*nf*', '*np*', and '*bf*' are used throughout the study to signify the related thermal and physical property/properties of the nanofluid, nanoparticles, and base−fluid, respectively.

The associated dimensional boundary conditions are as follows:

The outside walls of the enclosure,	(18)
Left side wavy wall $\overline{x} = G_1(\overline{y})$: $\overline{u} = \overline{v} = 0, \overline{T} = \overline{T}_0$	
Right side wavy wall $\overline{x} = G_2(\overline{y})$: $\overline{u} = \overline{v} = 0, \overline{T} = \overline{T}_0$	
Bottom side wall $\overline{y} = 0$: $\overline{u} = \overline{v} = 0, \frac{\partial \overline{T}}{\partial \overline{x}} = 0$	
Top side wall $\overline{y} = 0$: $\overline{u} = \overline{v} = 0, \frac{\partial \overline{T}}{\partial \overline{x}} = 0$	
The inner elliptic cylinder: $\overline{u} = \overline{v} = 0, \overline{T} = \overline{T}_1$	

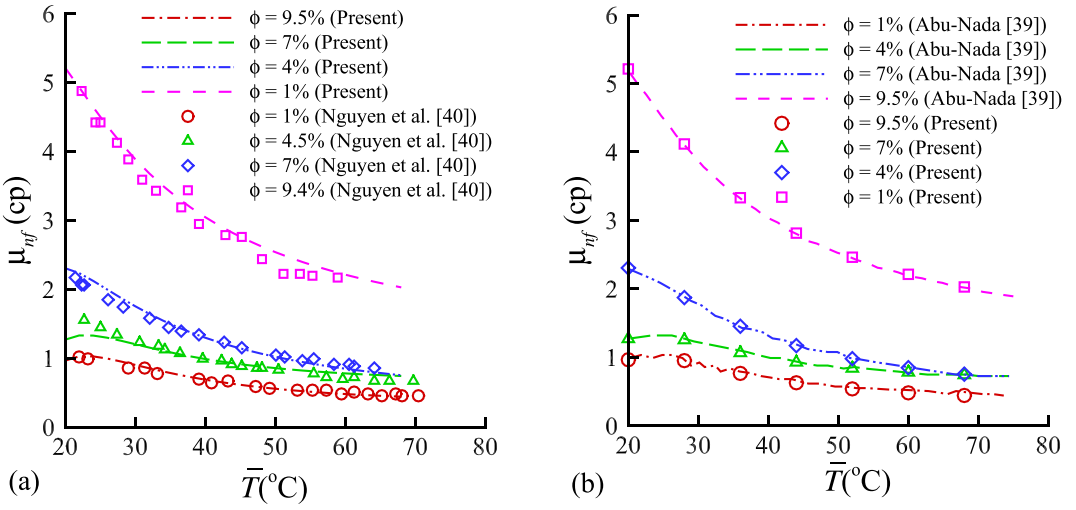

Fig. 2. Comparison of variable viscosity profile with (a) Nguyen et al. [40] and (b)Abu−Nada [39].

The following dimensionless parameters have been applied to convert resulting equations dimensionless,

$$u=\frac{\overline{u}L}{\alpha_{bf}}, v=\frac{\overline{v}L}{\alpha_{bf}}, x=\frac{\overline{x}}{L}, y=\frac{\overline{y}}{L}, T=\frac{\overline{T}-T_0}{\overline{T}_1-T_0}, p=\frac{L^2}{\rho_{nf}\alpha_{bf}^2}\overline{p}, \mu_{nf}=\frac{\overline{\mu}_{nf}}{\mu_{H_2O}} \tag{19}$$

Applying the dimensionless quantities of Eq. (19) into equation (2)–(4) and (18), we have

$$\frac{\partial u}{\partial x}+\frac{\partial v}{\partial y}=0 \tag{20}$$

$$\begin{aligned} u\frac{\partial u}{\partial x}+v\frac{\partial u}{\partial y}=&-\frac{\partial p}{\partial x}+\frac{1}{\rho_{nf}\alpha_f}\left(2\frac{\partial}{\partial x}\left(\mu\frac{\partial u}{\partial x}\right)+\frac{\partial}{\partial y}\left(\mu\frac{\partial u}{\partial y}+\mu\frac{\partial v}{\partial x}\right)\right)\\ &+\frac{\sigma_{nf}\rho_{bf}}{\sigma_{bf}\rho_{nf}}Ha^2\,\mathrm{Pr}\left(-u\sin^2\gamma+v\cos\gamma\sin\gamma\right)\end{aligned} \tag{21}$$

$$\begin{aligned} u\frac{\partial v}{\partial x}+v\frac{\partial v}{\partial y}=&-\frac{\partial p}{\partial x}+\frac{1}{\rho_{nf}\alpha_f}\left(2\frac{\partial}{\partial x}\left(\mu\frac{\partial u}{\partial x}\right)+\frac{\partial}{\partial y}\left(\mu\frac{\partial u}{\partial y}+\mu\frac{\partial v}{\partial x}\right)\right)\\ &+\frac{(\rho\beta)_{nf}}{\rho_{nf}\beta_{bf}}\mathrm{Pr}\,RaT+\frac{\sigma_{nf}\rho_{bf}}{\sigma_{bf}\rho_{nf}}Ha^2\,\mathrm{Pr}\left(-v\cos^2\gamma+u\sin\gamma\cos\gamma\right)\end{aligned} \tag{22}$$

$$u\frac{\partial T}{\partial x}+v\frac{\partial T}{\partial y}=\frac{(\rho c_p)_{nf}}{(\rho c_p)_{bf}}\left(\frac{\partial}{\partial x}\left(\frac{k_{nf}}{k_{bf}}\frac{\partial T}{\partial x}\right)+\frac{\partial}{\partial y}\left(\frac{k_{nf}}{k_{bf}}\frac{\partial T}{\partial y}\right)\right) \tag{23}$$

where, $\mu=\frac{\mu_{nf}}{\mu_{H_2O}}|\dot{\gamma}|^{(n-1)}$ and $|\dot{\gamma}|=\sqrt{2\left(\frac{\partial u}{\partial x}\right)^2+2\left(\frac{\partial v}{\partial y}\right)^2+\left(\frac{\partial u}{\partial y}+\frac{\partial v}{\partial x}\right)^2}$.

Pr, *Ra* and *Ha* are addressed as Prandtl number, Rayleigh number and Hartmann number, respectively and specified as,

$$\mathrm{Pr}=\frac{\nu_{bf}}{\alpha_{bf}}, Ra=\frac{g\beta(\overline{T}_1-T_0)L^3}{\nu_{bf}\alpha_{bf}} \quad \text{and} \quad Ha=LB_0\sqrt{\frac{\sigma_{bf}}{\mu_{bf}}} \tag{24}$$

The following expressions for the physical quantity ratios found in equation (21)–(23):

$$\begin{aligned} &\frac{1}{\rho_{nf}\alpha_{bf}}=\frac{1}{(1-\varphi)+\varphi b},\\ &\frac{(\rho\beta)_{nf}}{\rho_{nf}\beta_{bf}}=\frac{(1-\varphi)+\varphi bm}{(1-\varphi)+\varphi b},\\ &\frac{(\rho c_p)_{nf}}{(\rho c_p)_{bf}}=\frac{1}{(1-\varphi)+\varphi br},\\ &\frac{\sigma_{nf}\rho_{bf}}{\sigma_{bf}\rho_{nf}}=\frac{(d+2)+2(d-1)\varphi}{(d+2)-(d-1)\varphi}\frac{1}{(1-\varphi)+\varphi b}\end{aligned} \tag{25}$$

where, in equation (25)

$$d=\sigma_{np}/\sigma_{bf},\ \ b=\rho_{np}/\rho_{bf}, m=\beta_{np}/\beta_{bf} \ \text{ and } \ r=(c_p)_{np}\Big/(c_p)_{bf}$$

Following are the dimensionless representations of the boundary conditions:

The outside walls of the enclosure, (26)

- Left side wavy wall $x=G_1(y)$: $u=v=0, T=0$
- Right side wavy wall $x=G_2(y)$: $u=v=0, T=0$
- Bottom side wall $y=0$: $u=v=0, \frac{\partial T}{\partial x}=0$
- Top side wall $y=0$: $u=v=0, \frac{\partial T}{\partial x}=0$
- The inner elliptic cylinder: $u=v=0, T=1$

The following is a presentation of local Nusselt number around the surface,

$$Nu_L=-\frac{k_{nf}}{k_{bf}}\frac{\partial T}{\partial \eta} \tag{27}$$

where η indicates the angular coordinate. Nu_{avg} is computed by integrating equation (27) along the internal elliptic cylinder,

$$Nu_{avg} = \frac{1}{S}\int_0^S Nu_L d\eta \tag{28}$$

In Eq. (28), S indicates the surface area of the inner elliptic cylinder.

The stream function (ψ), which is generated from the velocity components u and v, is used to depict the fluid motion inside the considered enclosure. For 2D flows, the following relationship exists between the stream function (ψ) and velocity components (u, v) for 2D flows:

$$u = \frac{\partial \psi}{\partial y}, v = -\frac{\partial \psi}{\partial x} \tag{29}$$

These relations of the velocity components described in Eq. (29) for 2D flows lead to a single equation as follows,

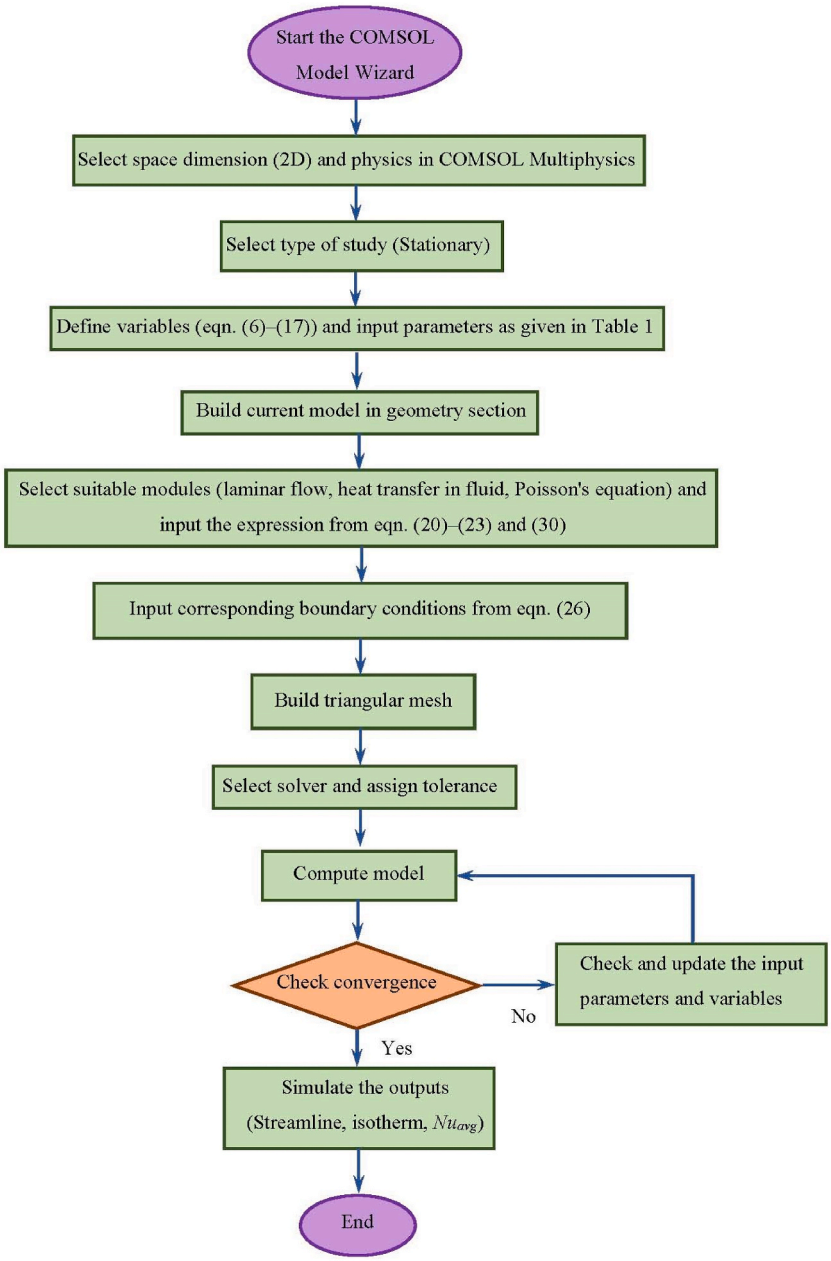

Fig. 3. Detailed process of the computational program in the COMSOL Multiphysics.

$$\frac{\partial^2\psi}{\partial x^2}+\frac{\partial^2\psi}{\partial y^2}=\frac{\partial u}{\partial y}-\frac{\partial v}{\partial x} \tag{30}$$

According to the abovementioned equation, the positive value of ψ signifies counterclockwise circulation, whereas the negative value of ψ indicates clockwise circulation.

3. Numerical methodology

The effect of MHD non-Newtonian Al_2O_3−water nanofluid between a wavy–shaped enclosure and a hot internal elliptic cylinder has been studied. The dimensionless set of the governing equations 20–23 and associated boundary conditions of Eq. (26) are numerically simulated using the COMSOL Multiphysics software, which is based on finite element methods. The laminar flow (spf) mode is applied to analyze single-phase fluid velocity in the laminar flow field, and the heat transfer (ht) at the fluid interface is used to model heat transfer by convection. Equation (30) is resolved by the Poisson's equation interface, and the stream function ψ is the result of that resolution. The physical model is constructed within the geometry application mode. A triangular mesh is fixed to generate a suitable mesh for the current physical model. The flow-chart of the computational technique is adequately explained in Fig. 3.

4. Grid independency test

Because of the variation in mesh size and mesh elements, the current model is numerically simulated to assess the effect of grid size on the consequences. In order to achieve the grid independent findings, several grids are verified for Nu_{avg} values around the hot inner corrugated cylinder. The computed results for various mesh sizes are presented in Table 2. To run this model, an extremely fine mesh with a mesh element of 29322 has been chosen. The resulting outcomes are good enough to obtain precise results.

5. Validation of numerical solutions

Code validation of the existing study is compared with the results determined by Turan et al. [43] as specified in Fig. 4 for the case of natural convective flow of non-Newtonian power law fluids in a one side heated square–shaped enclosure. In general, the result has a decent agreement with current work data. The comparison results of Nu_{avg} are examined for $Ra = 10^4$ and 10^5, $Ha = 0$, $\varphi = 0.0$, Pr = 100 and power law index, n = (0.8 to 1.8). To further check the precision of the existing numerical code, another validation is performed using the work of Ghasemi et al. [44]. In this instance, the approximate data of Nu_{avg} is double-checked against the numerical calculation for distinct Hartmann number and solid volume fraction of nanoparticles. These results have a good level of accuracy with Ghasemi et al. [44], as seen in Table 3. For the model validation, the present work is compared with the previous published numerical and experimental results presented by Cesinini et al. [45]. They experimentally and numerically studied the heat transfer by natural convection from a horizontal cylinder enclosed in a rectangular cavity. In Table 4, Cesini et al. [45]'s experimental and numerical results for Nuavg are cross-checked with the numerical calculation for distinct Rayleigh number and aspect ratio of the enclosure. From Tables 4 and it can be detected that the obtained data agree well with Cesini et al. [45].

It is noted that the physical model of the present study will take the same form as that of Cesini et al. [45], if we assume $\alpha_1 = 0$ and $\alpha_2 = 0$ in equation (1), considering the inner ellipse as a circular cylinder and the outer enclosure as a rectangle, and the cavity filled with air. In addition, the power law index, n = 1.0, magnetic field intensity, Ha = 0, volume fraction of nanoparticles, φ = 0.0. Moreover, the boundary conditions will represent the isothermal case of Cesini et al. [45] if we are considering the heat flux condition for the top wall of the enclosure. From this perspective, the current numerical code can be regarded as entirely trustworthy.

6. Results and discussion

The consequence of a magnetic field on a non-Newtonian nanofluid between an enclosure is examined in this paper. The study's geometry is considered as a complex wavy shaped enclosure with an inclined elliptic cylinder in the middle of the enclosure. Al_2O_3−water nanofluid is used to fill the enclosure. The temperature of the enclosure's two horizontal walls is considered adiabatic

Table 2
Result of grid independency check for $n = 0.8$, $\varphi = 0.04$, $Ra = 10^5$, $Ha = 10$, $\omega = 135°$, $\gamma = 45°$ and Pr = 6.57.

Mesh Size	Mesh Elements	Nu_{avg}
Extremely Coarse	588	13.293
Extra Coarse	858	13.367
Coarser	1374	13.470
Coarse	2108	13.484
Normal	2696	13.466
Fine	4030	13.477
Finer	8726	13.475
Extra Fine	22690	13.485
Extremely Fine	29322	13.482

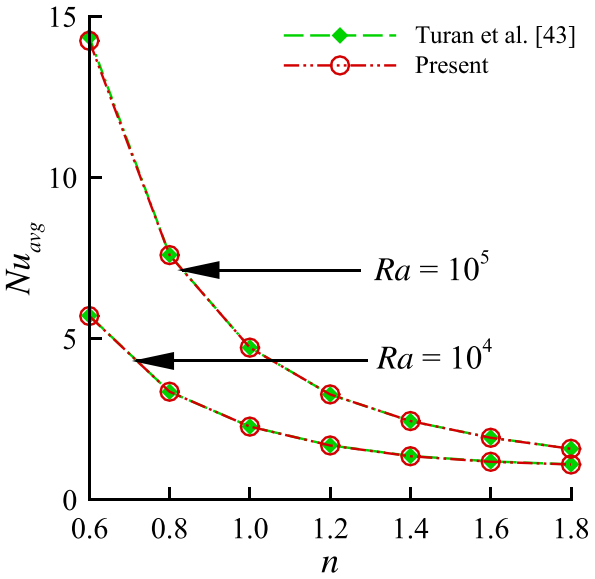

Fig. 4. Comparison of the current simulation result with the graphical expression of Turan et al. [43] for Nu_{avg} against n.

Table 3
Comparison of Nu_{avg} of the current study with Ghasemi et al. [44].

		$Ha = 0$	$Ha = 15$	$Ha = 30$	$Ha = 45$	$Ha = 60$
$\varphi = 0.0$	Ghasemi et al. [44]	4.738	4.143	3.150	2.369	1.851
	Present work	4.7218	4.1284	3.1394	2.3618	1.8455
$\varphi = 0.02$	Ghasemi et al. [44]	4.820	4.179	3.138	2.342	1.831
	Present work	4.8041	4.1658	3.1281	2.3353	1.8257
$\varphi = 0.04$	Ghasemi et al. [44]	4.896	4.211	3.124	2.317	1.815
	Present work	4.8814	4.1986	3.1147	2.3104	1.8110
$\varphi = 0.06$	Ghasemi et al. [44]	4.968	4.239	3.108	2.293	1.806
	Present work	4.9537	4.2270	3.0994	2.2876	1.8024

Table 4
Comparison of Nu_{avg} of the current study with the experimental and numerical data of Cesini et al. [45].

		Aspect Ratio = 2.1			Aspect Ratio = 2.9			Aspect Ratio = 3.6		
		present	calc.	exp.	present	calc.	exp.	present	Calc.	exp.
Ra	1.3×10^3	2.33	2.36	2.46	2.25	2.25	2.54	2.36	2.35	2.35
	2.4×10^3	2.61	2.61	2.80	2.66	2.65	3.00	2.73	2.75	2.79
	3.4×10^3	2.82	2.77	3.07	2.92	2.90	3.15	2.96	2.98	3.06

while the vertical wavy walls are kept at a constant cold temperature. The elliptic-shaped inner cylinder is considered to be heated. The physical and theoretical explanation of the obtained results and their graphical statement for several values of parameters like Rayleigh number (Ra), Hartmann number (Ha), magnetic field orientation angle (γ), rotation angle of the inner cylinder (ω), power law index (n) and solid volume fraction of nanoparticles (φ) are reported in the following segments.

Fig. 5(a)–(l) depict the streamlines for various Ra and n. The pertinent parameters are considered as $\varphi = 0.04$, $Ha = 10$, $\omega = 135^\circ$, $\gamma = 45^\circ$ and $\mathrm{Pr} = 6.57$ to explain the flow act for different Ra (10^3, 10^4, 5×10^4 and 10^5) and n (0.8, 1.0 and 1.4). At $n = 0.8$, maximum values of stream function for $Ra = 10^3$, 10^4, 5×10^4 and 10^5 are (0.44, 3.92, 10.38 and 13.90), respectively. From the expression of Ra in equation (24), it is seen that Ra is directly connected to natural convection. So, increasing Ra causes an improvement in natural convection and fluid flow becomes stronger. Fig. 5(a)–(l) show that increasing Ra causes the value of the streamlines intensity to increase. Meanwhile, when examining Fig. 5(a)–(d), it can be observed that heat transfer occurs quickly and the intensity of fluid flow is greater when the influence of viscosity is reduced ($n = 0.8$). But increasing n, reduces the fluid's viscosity instantly. Due to this reason, the reverse scenario is observed from Fig. 5(i)–(l) when the viscosity is high ($n = 1.4$). Because of the central heating source (hot elliptic cylinder) and the right and left walls being uniformly cooled, the non-Newtonian nanofluid inside the enclosure continues to thin and rises adjacent to the side of the heated cylinder and flows moving down along the cooled side walls. Consequently, this phenomenon generates a double circulation. In Fig. 5(a), (c)–(e), (h)–(k), one of these circulations covers the right lower part of the

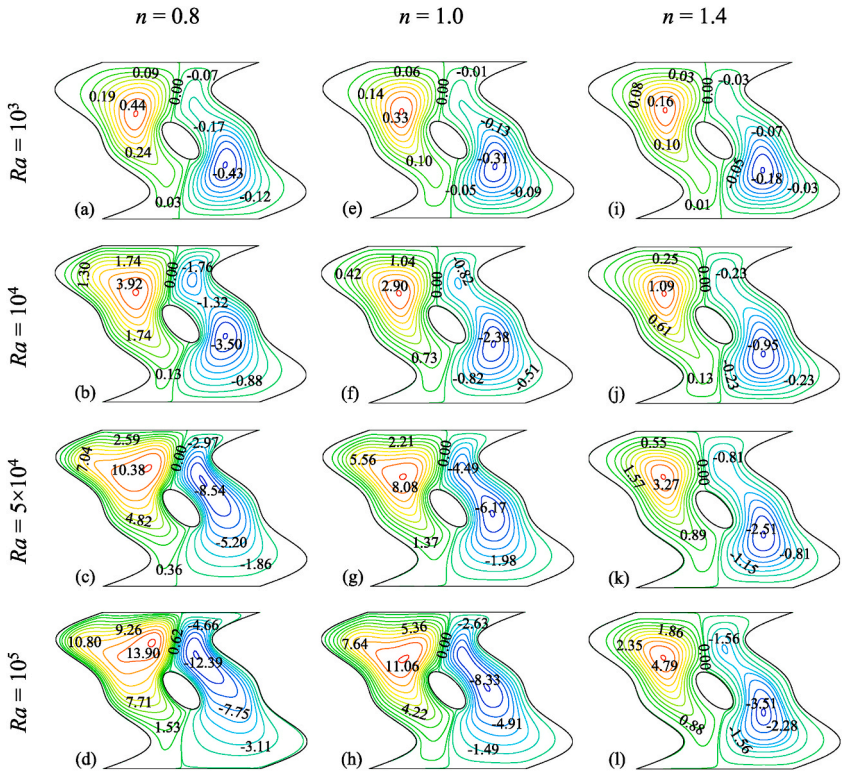

Fig. 5. Streamlines for several *Ra* and *n* at $Ha = 10$, $\varphi = 0.04$, $\gamma = 45^\circ$, $\omega = 135^\circ$ and Pr = 6.57.

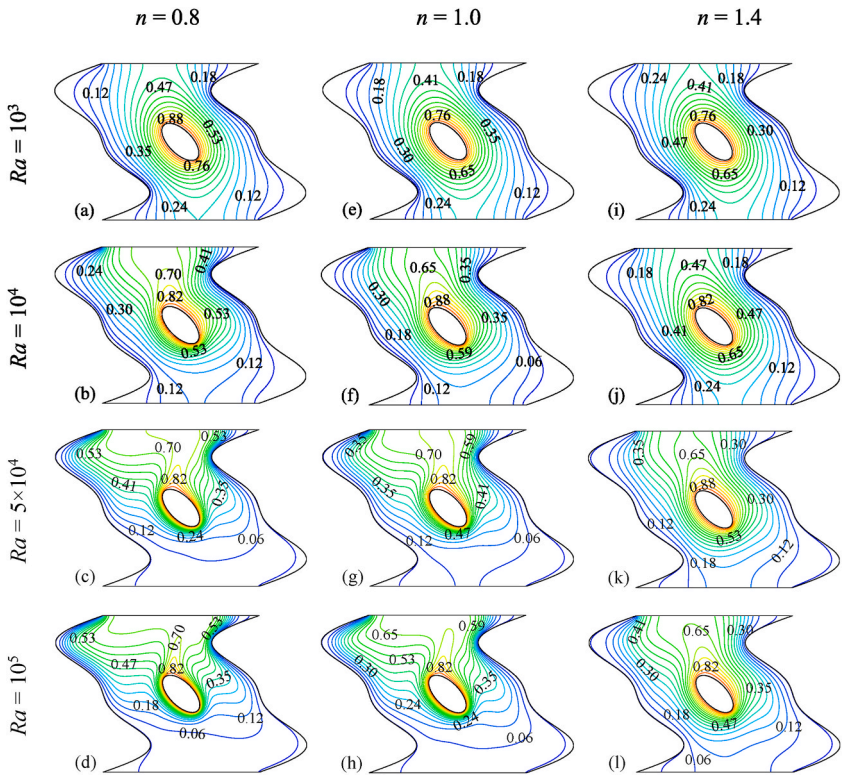

Fig. 6. Isotherm contours for several *Ra* and *n* at $\varphi = 0.04$, $Ha = 10$, $\gamma = 45^\circ$, $\omega = 135^\circ$ and Pr = 6.57.

enclosure and moves in a clockwise direction creating a main vortex. Another one appears in the enclosure's upper left corner and the second circulation moves in an anticlockwise direction. At Fig. 5(b), (f), (g) and (l) there is also a minor vortex is appeared in the upper right corner. With varying the range of *Ra*, the size and position of the vortex are changed. The vortex takes on a new shape, becoming elliptic and larger in size.

In Fig. 6(a)−(l), the isotherm profile is illustrated for the same values as in Fig. 5. The isotherm pattern shown in Fig. 6(a)–(l) varies with *Ra* and *n*. At smaller *Ra*, for all values of *n* (*n* = 0.8, 1.0 and 1.4) the distribution of the isotherm contours are regular. But it continued to wavy for a larger *Ra* (Fig. 6(c), (d), (g), (h), (k) and (l)). This phenomenon indicates that conduction is the core fact of thermal diffusion at lower *Ra*. The graphical representation of this phenomenon is observed in Fig. 6(a), (e) and (i). The buoyancy force is strengthened by a higher *Ra*, causing natural convection to become the major mechanism of heat transfer. Due to the hot cylinder, the rate of thermal diffusion around the elliptical cylinder area and the upper part of the enclosure is relatively high. This is why for higher *Ra*, the density of the isotherm contours near the heated cylinder is enhanced, indicating that the heat release from the heated elliptical cylinder is increased. Then, the isothermal contours turn more irregular with boosted Ra and a smaller n. Fluid flow adjacent to the wavy wall is comparatively slower than in the upper portion of the enclosure. The heat transfer rate is lower towards the corrugated wall because of the cooler wall. Moreover, in the Newtonian (*n* = 1.0) and shear thickening (*n* = 1.4) phase for all values of *Ra*, the isotherm contours are regular. This is because of higher viscosity of non-Newtonian nanofluid. As the viscosity has a direct relation with flow behavior index (*n*).

To examine the significance of *Ha* on streamlines and isotherm profiles for distinct values of *n* have been presented in Fig. 7(a)− (l) and 8(a)–(l), respectively. In Fig. 7(a)–(d), the strengths of the streamlines, represented by *Ha* values of 0, 10, 20, and 40, are observed to be (21.43, 13.90, 8.66, and 3.62) respectively, for the case where *n* is equal to 0.8. When examining the streamline patterns shown in Fig. 7(e)–(h) and 7(i)–(l), it is evident that the intensity of the flow decreases within the enclosure as the values of *Ha* and *n* become larger. *Ha* signifies the magnetic field and which depends on Lorentz's force. Lorentz's force has the inverse effect of buoyancy force. The strength of the fluid circulation is downgraded as a result of higher *Ha*. Thus, the convection effect is reduced due to an increase in Lorentz force. The fluid's viscosity gets attenuated and the vorticity magnitude reduces for rising the power law index (*n*). Higher values of *n* slow down fluid motion in the cavity. At *Ha* = 0 and *n* = 0.8, two vortices are formed on the enclosure's upper portion. Keeping *n* fixed, the increment of *Ha* causes the right–side vortex to start moving down in direction. In Fig. 7((c), (d), (g), (h), (k) and (l)), a minor vortex is also visible in the upper right corner. This phenomenon is caused by higher *Ha* and *n*, which reduces flow intensity and weak fluid movement. It is monitored from Fig. 8(a)−(l) that, the thermal patterns are spread inside the cavity and become regular around the heated cylinder and cold walls as *Ha* goes down. However, in Fig. 8(a)–(d) and 8(e)–(h), when considering *Ha*

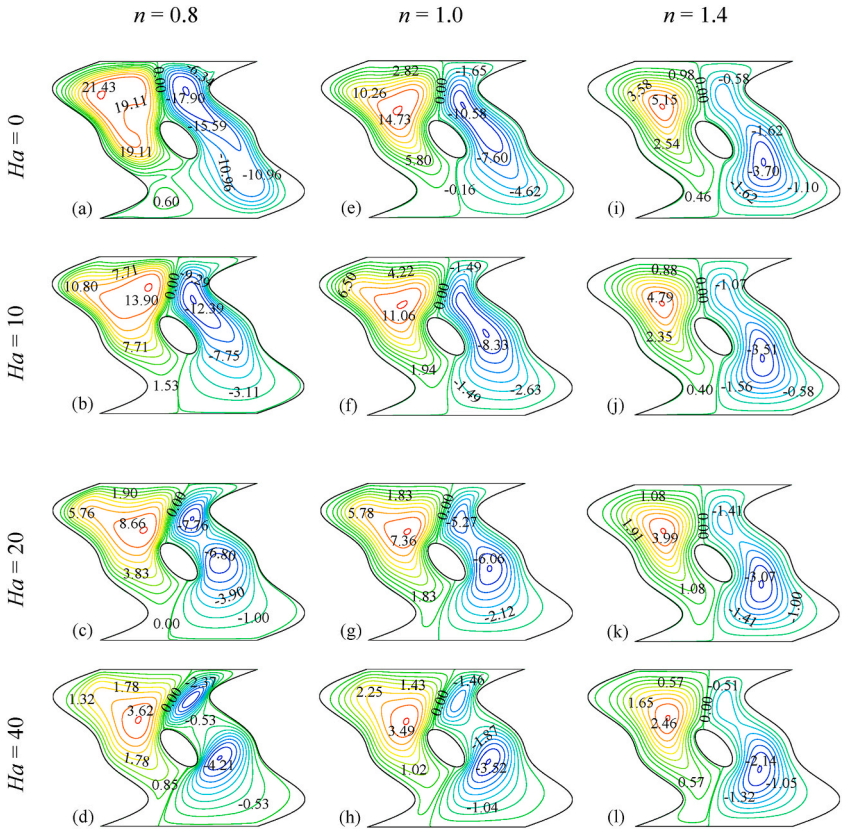

Fig. 7. Streamlines for several *Ha* and *n* at $Ra = 10^5$, $\varphi = 0.04$, $\gamma = 45°$, $\omega = 135°$ and Pr = 6.57.

values of 0, 10, 20, and 40 along with n value of 0.8 and 1.0, it can be observed that the isotherm contours exhibit undulations in the upper region of the enclosure. By analyzing Fig. 8(i)–(l) while considering a value of n equal to 1.4, it can be concluded that the distribution of the isotherm contours becomes more regular. The reason for this is the Lorentz force and builds up the viscous effect, which slows down fluid movement.

Figs. 9(a)−(l) and 10(a)−(l) show the development of the streamlines and isotherms distribution by increasing γ and n at $\varphi = 0.04$, $Ra = 10^5$, $Ha = 10$, $\gamma = 45^\circ$ and Pr = 6.57. In Fig. 9(a)–(d), maximum values of streamline magnitude are detected for $\gamma = 0^\circ$, 15°, 45° and 90° are 14.62, 14.34, 13.90 and 14.01, respectively for $n = 0.8$. Within Fig. 9(e)–(h), for the case of a Newtonian nanofluid ($n = 1.0$), the maximum rate of streamline magnitude is recorded at $\gamma = 0^\circ$, 15°, 45° and 90° are 12.03, 11.62, 11.06 and 11.63. When considering the cases of shear thickening ($n = 1.4$), observations from Fig. 9(i)–(l) reveal that the highest magnitude of the stream function is recorded at γ angles of 0°, 15°, 45°, and 90°, with values of 4.85, 4.82, 4.79, and 4.87 respectively. Fig. 9(a)–(l) reveal that the values of the stream function magnitude decrease as a result of increasing n and γ (except $\gamma = 90^\circ$). At $n = 0.8$, two major vortices become visible at different locations and of dissimilar size. But for all considered values of γ and $n = 1.4$, one minor vortex is visible on the right top portion of the cavity. The vortices are changing their shape slowly and switching their position and size. The change is more noticeable on the right part of the enclosure compared to the left portion of the cavity. When analyzing Fig. 10(a)–(d), 10(e)–(h), and 10(i)–(l), considering γ values of 0°, 15°, 45°, and 90°, in combination with n values of 0.8, 1.0, and 1.4, respectively, it becomes noticeable that the thermal patterns change very slowly inside the cavity and gradually become regular around the heated cylinder and the cold walls as n increases. The reason for this is the magnetic field orientation angle and the amplification of the viscous effect, which slows down fluid motion. The impact of γ on isotherm contours is relatively less significant for higher values of n.

Several values of ω have been used in Figs. 11(a)−(l) and 12(a)−(l) to determine the effect of ω and n on streamlines and thermal patterns at $\varphi = 0.04$, $Ra = 10^5$, $Ha = 10$, $n = 0.8$, $\gamma = 45^\circ$ and Pr = 6.57. In Fig. 11(a)–(d), for $n = 0.8$, maximum and minimum values of stream function are detected for $\omega = 45^\circ$ (is 15.06) and 135° (is 13.89), respectively. From Fig. 11(e)–(h), at $n = 1.0$, maximum and minimum values of stream function magnitude are noted for $\omega = 45^\circ$ (is 11.6) and 135° (is 11.07). When observing Fig. 11(i)–(l) for the case of $n = 1.4$, the highest and lowest rates of stream function are recorded at $\omega = 45^\circ$ (is 5.31) and 135° (is 4.79), respectively. The rotation angle of inner cylinder (ω) of the inner elliptic cylinder has a regular control on the value of the stream function profile and thermal pattern. In Fig. 11(b), (f), (g) and (i)−(l) there exist two major and one minor vortices. But in Fig. 11 (a), (c)–(e) and (h) contain only two major vortices. The vortices are varying their shape, shifting their position and changing their size. This is happening because of the different rotation angle of the inner cylinder. By examining Fig. 11(a)–(d), 11(e)–(h), and 11(i)–(l), the corresponding ω values of 0°, 45°, 90°, and 135° are taken into account, along with the respective n values of 0.8, 1.0, and 1.4, it is scrutinized that higher values of ω result in thicker the thermal patterns adjacent to the wavy walls of the enclosure and nearly the lower part of the hot internal elliptic cylinder. Moreover, isotherm contours at the topmost part are randomly spread because of the different rotation angle.

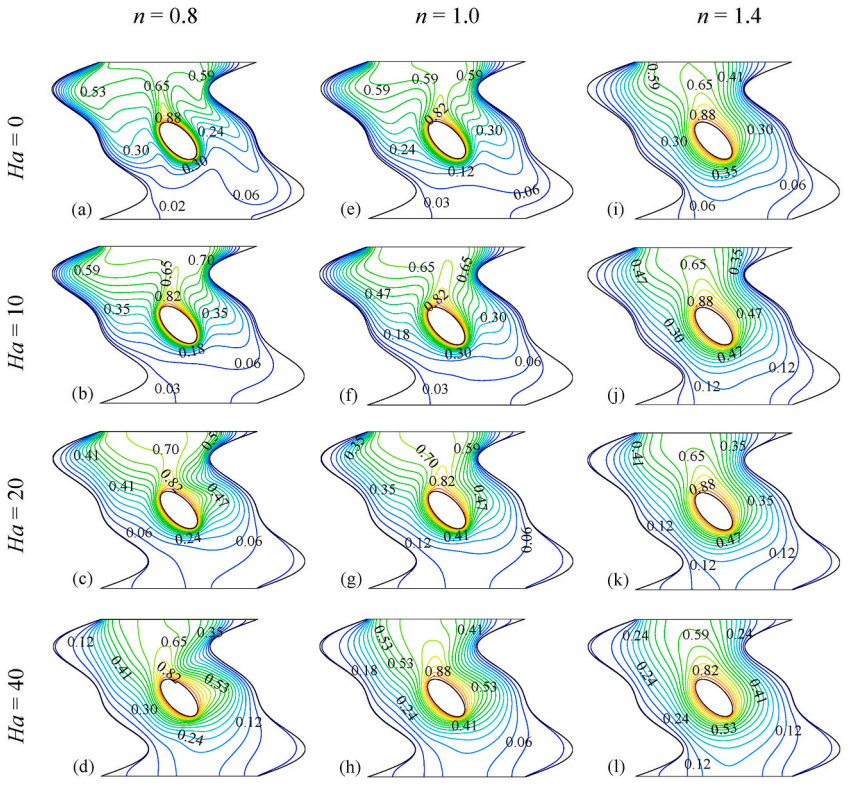

Fig. 8. Isotherm contours for several Ha and n at $Ra = 10^5$, $\varphi = 0.04$, $\gamma = 45^\circ$, $\omega = 135^\circ$ and Pr = 6.57.

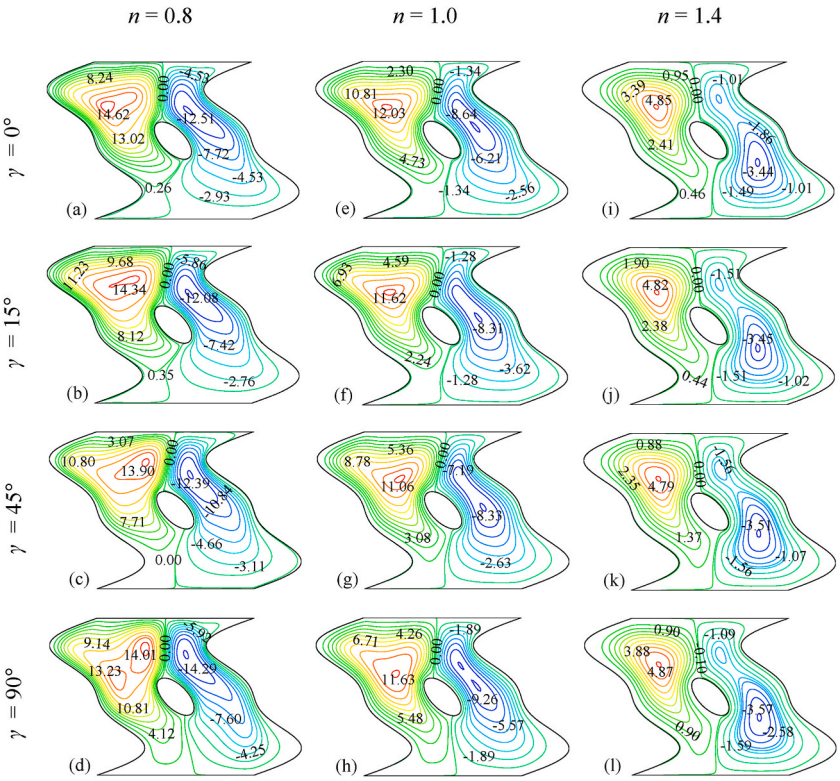

Fig. 9. Streamlines for several γ and n at $Ra = 10^5$, $Ha = 10$, $\varphi = 0.04$, $\omega = 135^\circ$ and Pr = 6.57.

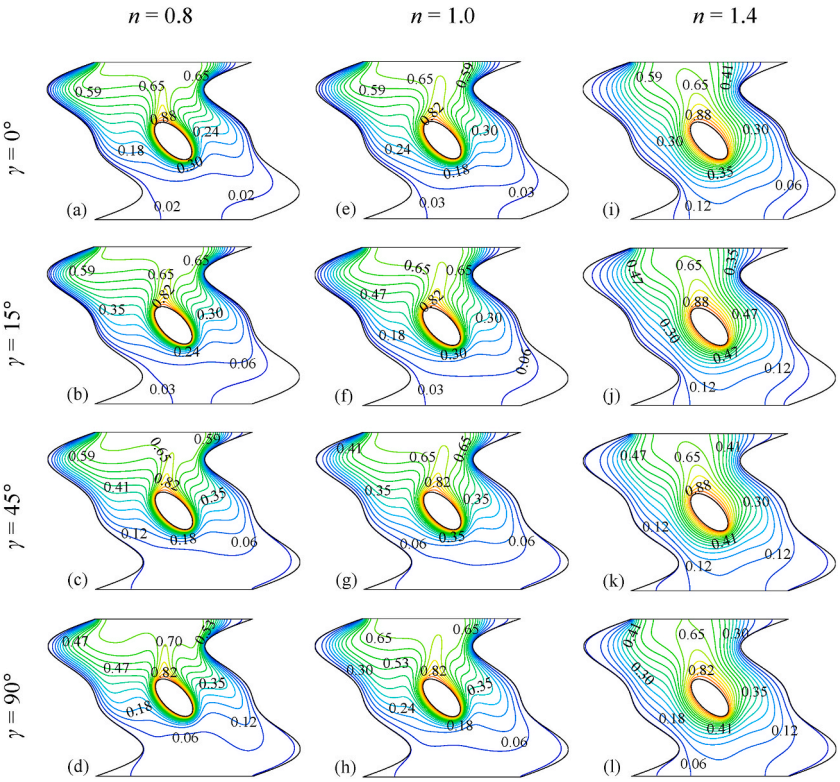

Fig. 10. Isotherm contours for different γ and n at $Ra = 10^5$, $Ha = 10$, $\varphi = 0.04$, $Ra = 10^5$, $Ha = 10$, $\omega = 135^\circ$ and Pr = 6.57.

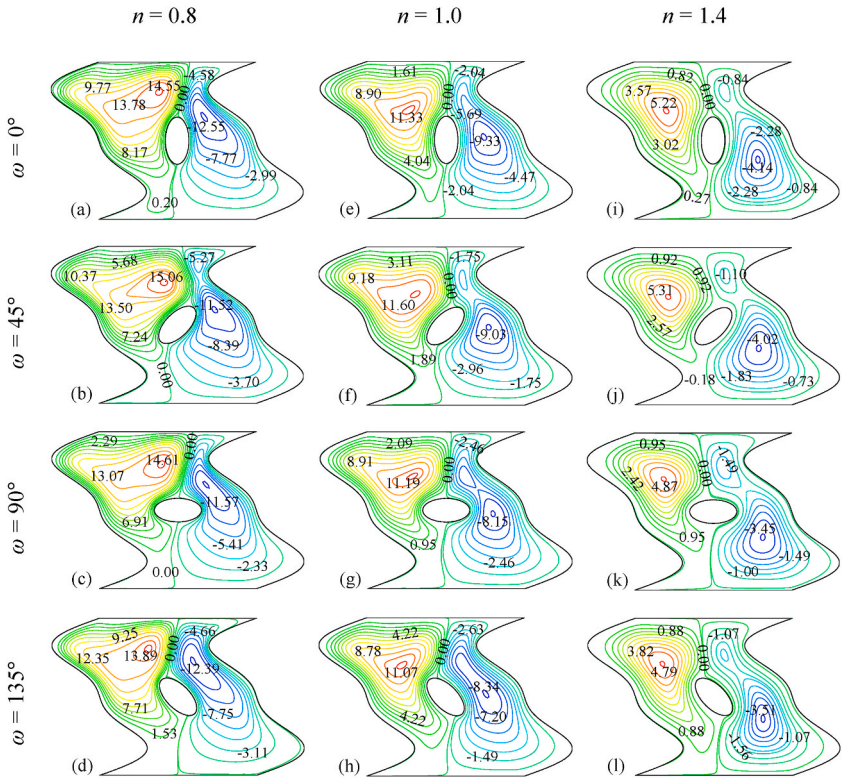

Fig. 11. Streamlines for different ω and n at $Ra = 10^5$, $Ha = 10$, $\varphi = 0.04$, $\gamma = 45^\circ$ and Pr = 6.57.

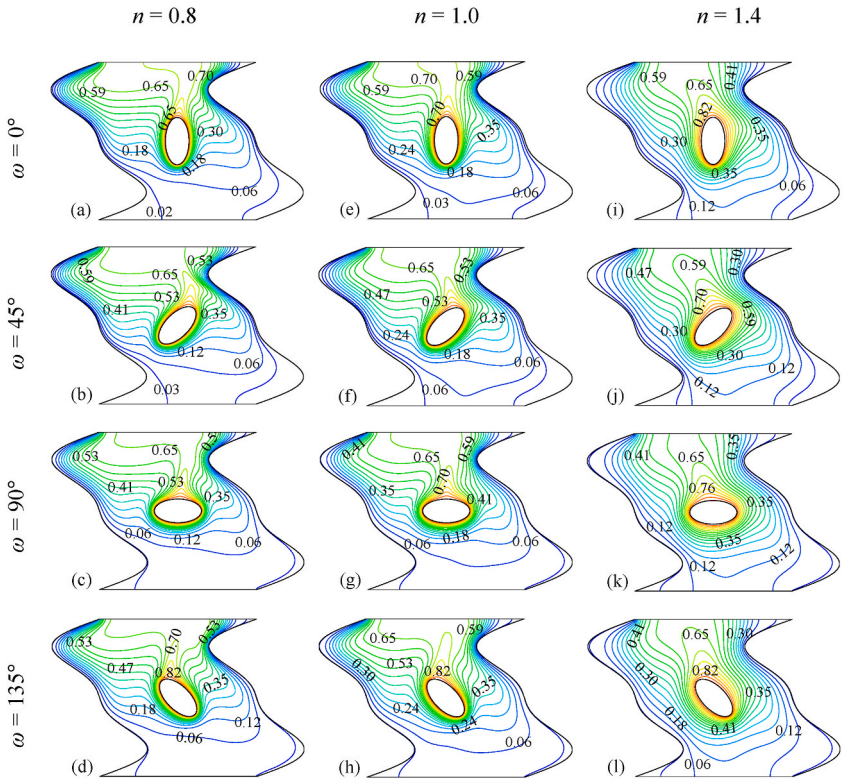

Fig. 12. Isotherm contours for different ω and n at $Ra = 10^5$, $Ha = 10$, $\varphi = 0.04$, $Ra = 10^5$, $Ha = 10$, $\gamma = 45^\circ$ and Pr = 6.57.

Fig. 13(a)–(l) present the strength of the power law index (n) and the concentration ratio of nanoparticles (φ) on streamlines. To figure out the controlled of power law model on the fluid's heat transfer rate, power law model is simulated by changing n to characterize the shear dependent viscosity. In Fig. 13(a)–(d), when considering the case of shear thinning case ($n = 0.8$), it is observed that viscosity of fluid reduces and flow intensity increases. However, in the case of shear thickening ($n = 1.4$), as depicted in Fig. 13(i)–(l), there is an increase in fluid viscosity, which leads to a decrease in flow intensity. So, the reduction of the power law index for non-Newtonian nanofluids means that the effective viscosity of the fluid is declining. As a result, the fluid becomes thinner and the flow becomes faster. Because of this, the movement of fluid becomes more intense. So, heat transfer rate also intensifies and momentum boundary layer thickness decreases too. The fluid's viscosity becomes attenuated and the vorticity magnitude rises. Thus, a smaller power law index accelerates fluid motion in the enclosure. The opposite phenomenon is revealed for $n > 1$. The maximum and minimum values of streamlines at $\varphi = 0.04$, are detected for $n = 0.8$ (is 13.90), 1.0 (is 11.06) and 1.4 (is 4.79), respectively. In Fig. 13 (a), value of vorticity magnitude for $\varphi = 0.00$ is 14.01 when Al_2O_3 nanoparticles are not mixed with base fluid. Afterward, nanoparticles of $\varphi = 0.01$ concentration are joined together with base fluid vorticity intensity, which generates lower values (13.9) compared to the case of $\varphi = 0.0$ and it turns into minimum (13.87) for a concentration of $\varphi = 0.03$ nanoparticles. It indicates that the solid volumetric concentration of nanoparticles weakens the fluid movement at greater values of φ. The reason behind the case is that combining nanoparticles (Al_2O_3) in a base fluid (water) augments the concentration of nanofluid, so the intensity of nanofluid circulation diminishes due to the intensification of the concentration of nanoparticles. The maximum values of $|\psi|$ for higher n with increasing φ are also reducing compared to the maximum value of $|\psi|$ at smaller n. For small n (Fig. 13(a)–(h)), two vortices of opposite direction appear and position of the vortex is at the top of the left and right−side layers. But as n grows (Fig. 13(i)–(l)), a minor vortex appears at the right upper part of the enclosure for non-Newtonian shear thickening fluid ($n = 1.4$). The major vortex on the right side is moving down into the enclosure. Vortices are taking on a new shape, becoming round and smaller in size.

The influence of different ratios of φ on the thermal contours of a wavy enclosure for different n is depicted in Fig. 14(a)−(l). By analyzing Fig. 14(a)–(d), it is apparent that the isotherm of different nanoparticle concentrations is strongly affected by lower n ($n = 0.8$). This occurs because a smaller power law index intensifies the fluid movement by reducing the viscous effect of non-Newtonian nanofluid. Moreover, shear thinning non-Newtonian nanofluid leads to better development in the convective heat transfer rate. With increasing φ, the thermal conductivity of nanofluid also boosts up. So, isotherm contours become more irregular and wavier with increasing φ and smaller n. Isotherm counters adjacent to the upper wavy wall and lower part of the hot cylinder are comparatively denser than in the upper part of the cavity. From Fig. 14(e)–(h) it is detected that, with the growth of the power law index (n=1.0), fluid flow is reducing gradually for higher φ. In Fig. 14(i)–(l), the thermal patterns are regular closer to the heated cylinder and nearly identical for a variety of the larger values of φ and n ($n = 1.4$).

To figure out the control of Hartmann number (Ha) on heat transfer rate from Newtonian ($n = 1.0$) and non−Newtonian ($n = 0.8$ and 1.4) phases for different Ra and ω have been chosen in Figs. 15(a)−(c) and (a)−(c), respectively. This graph represents the progress of Nu_{avg} when exposed to a strong magnetic field. Lower values of Ra ($Ra = 10^3$) and ω ($\omega = 0^\circ$) present that the values of Nu_{avg} are comparatively low for all stages of n (except $n = 1.4$). But the situation is gradually upgraded with rising the scale of Ra but rapidly reduced with higher n. The viscosity of fluid increases with rising n and it shifts from the shear thinning phase to the share thickening stage. Moreover, the strength of the magnetic field boosts as Ha rises. But Lorentz force has an opposite effect to the buoyancy. All the above factors, cause a reduction in the flow's intensity. But rising Ra boosts the convection flow and positively changes the thermal field. In addition, mounting Ha decays all the positive influence of Ra and ω. In the absence of magnetic field, heat transfer rate is maximum for larger Ra. But rising Ha creates a reduction in Nu_{avg}. At $Ha = 0$, the average Nusselt number is at its maximum for $Ra = 10^5$ in a shear thinning case. But at $n = 1.4$ (shear thickening), value of Nu_{avg} decreases much for $Ra = 10^5$. For all Ha, value of Nu_{avg} is maximum for $\omega = 45^\circ$ and minimum for $\omega = 135^\circ$. The scenario has changed for Newtonian and shear thickening fluid (Fig. 16(b) and (c)). The rotation angle of the inner cylinder (ω) of the inner elliptic cylinder has an irregular control on the value of the heat transfer rate.

The graphical expressions in Fig. 17(a)−(c) present the development of Nu_{avg} for non-Newtonian and Newtonian nanofluid for distinct values of the rotation angle of inner cylinder (ω) via changing Ra. Generally, at higher Ra (stronger buoyancy force), natural convection increases inside the enclosure and heat moves faster from one place to another. The growth of Ra thus causes Nu_{avg} to increase. But Nu_{avg} started to reduce for greater n. The fluid movement is increased by the shear-thinning fluid ($n < 1$), while the shear-thickening fluid ($n > 1$) starts to slow the flow of the fluid. At higher Ra, the heat transfer rate is maximum for $\omega = 0^\circ$ and minimum for $\omega = 90^\circ$ (Fig. 17(a)). In the presence of greater Ra and $\omega = 0^\circ$, the convective heat transfer rate at $n = 0.8$ increases more effectively. For Newtonian and non-Newtonian phases of nanofluids, ω has an asymmetrical impact on the rate of heat transfer.

Fig. 18(a)−(c) represent the distribution of Nu_{avg} along the hot cylinder for distinct values of Ra with changing the range of particle volume concentration, φ for non-Newtonian and Newtonian nanofluids. Graphs 18(a) and (b) show that a higher Ra value and adding 1% nanoparticles to a base fluid result in greater heat transfer performance. But increasing nanoparticles by more than 1% causes a decline in heat transfer rates. This is also true for $n = 1.0$ ($Ra = 10^4 - 10^5$). It shows that the greater values of solid volumetric concentration ($\varphi > 0.01$) of nanoparticles is weaken the heat transfer rate. This is happening in three different aspects. Firstly, the development of thermal conductivity with increasing φ. Secondly, the enhancement of effective viscosity with changing φ. As, φ dependent viscosity and thermal conductivity are chosen in this study. Lastly, the increment of the power law index, n. The aforesaid factors can cause distinct impacts. The first one directly produces heat transfer intensification. The second reduces heat exchange rate via boosting viscus resistance. The last one upgrades the viscosity of nanofluid. A lower value of n leads to a decrease in the viscosity profile. But viscosity started to increase for greater n. Combining nanoparticles (Al_2O_3) in base fluid augments the concentration of nanofluid, so the intensity of non-Newtonian nanofluid circulation diminishes due to the intensification of the concentration of nanoparticles. Therefore, Nu_{avg} becomes more significant with increasing Ra and φ at the non−Newtonian shear thinning stage.

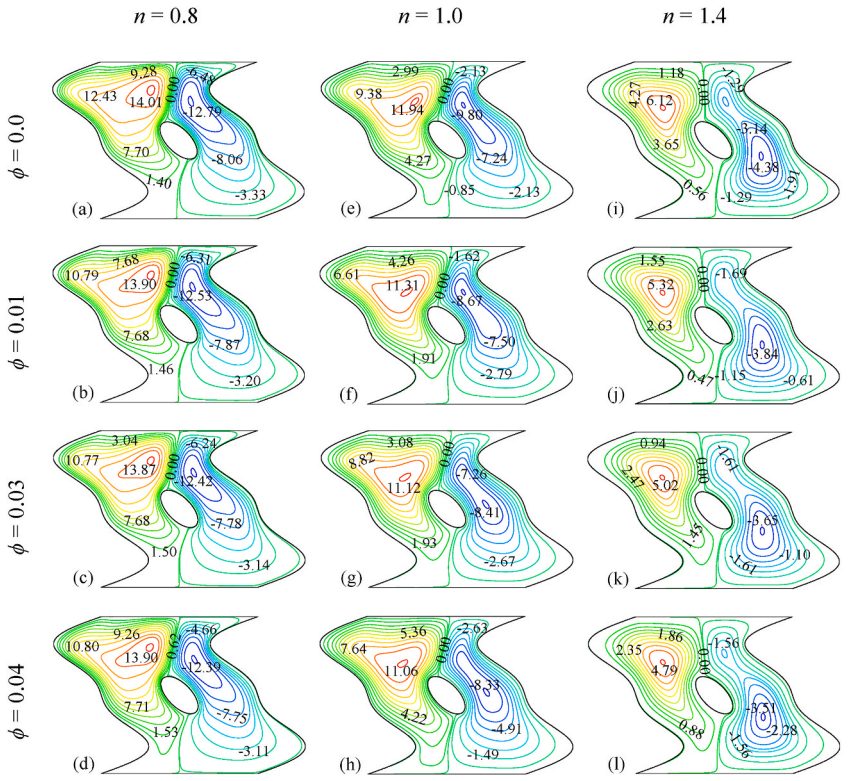

Fig. 13. Streamlines for different n and φ at $Ra = 10^5$, $Ha = 10$, $\gamma = 45^\circ$, $\omega = 135^\circ$ and Pr = 6.57.

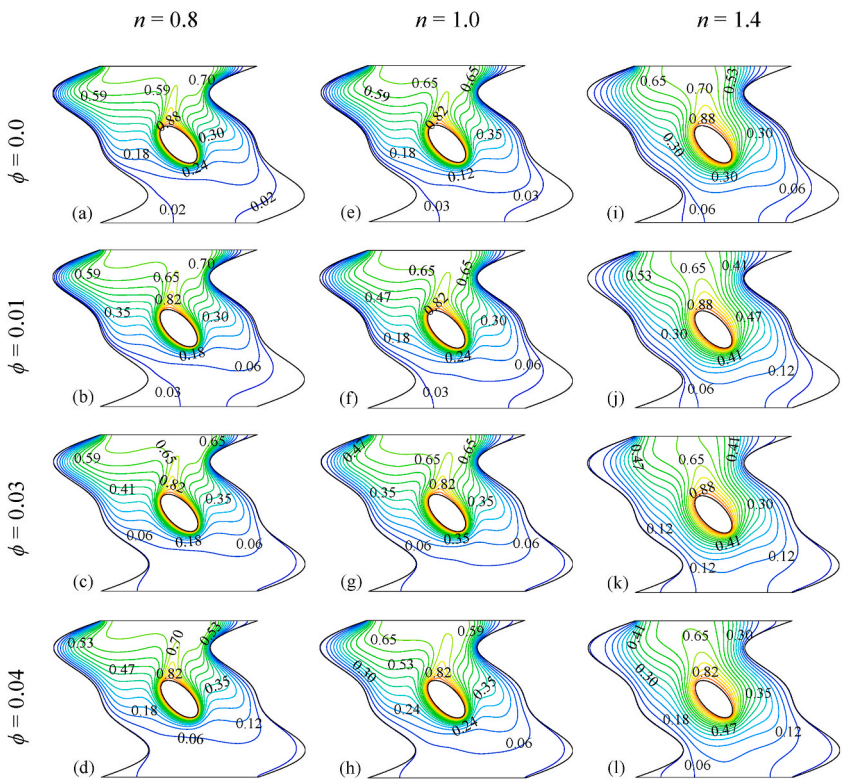

Fig. 14. Isotherm contours for different φ and n at $Ra = 10^5$, $Ha = 10$, $\gamma = 45^\circ$, $\omega = 135^\circ$ and Pr = 6.57.

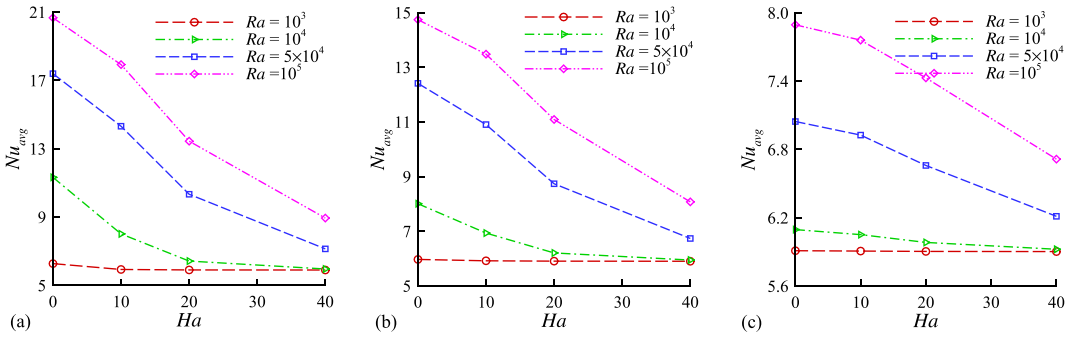

Fig. 15. Nu_{avg} versus Hartmann number (Ha) for several Ra for (a) $n = 0.8$ (b) $n = 1.0$ and (c) $n = 1.4$ at $\varphi = 0.04$, $\gamma = 45^{\circ}$, $\omega = 135^{\circ}$ and Pr = 6.57.

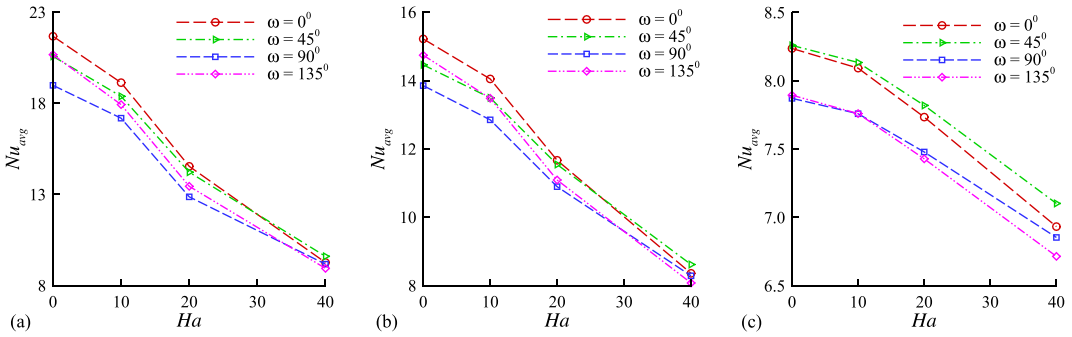

Fig. 16. Nu_{avg} versus rotation angle of inner cylinder (ω) for several Ha for (a) $n = 0.8$ (b) $n = 1.0$ and (c) $n = 1.4$ at $Ra = 10^5$, $\varphi = 0.04$, $\gamma = 45^{\circ}$ and Pr = 6.57.

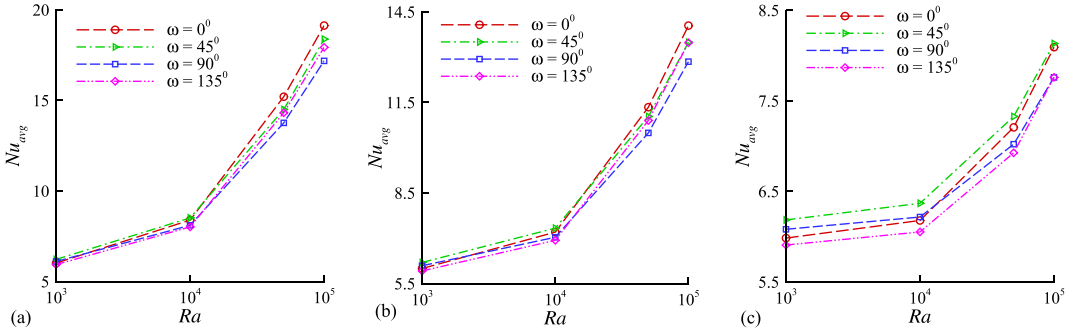

Fig. 17. Nu_{avg} versus rotation angle of inner cylinder (ω) for several Ra for (a) $n = 0.8$ (b) $n = 1.0$ and (c) $n = 1.4$ at $Ha = 10$, $\varphi = 0.04$, $\gamma = 45^{\circ}$ and Pr = 6.57.

The graphical expressions in Fig. 19(a)–(c) present the development of Nu_{avg} for non-Newtonian and Newtonian phases for distinct Ha via changing the value of the concentration ratio of nanofluid (φ). It is seen from Fig. 19(a)–(c) that a lower value of n leads to an increase in Nu_{avg} profile. But Nu_{avg} started to reduce for greater n. The outcomes show that heat transfer is fast and intensity of the fluid flow is better when the viscous effects are low ($n = 0.8$). It is also seen that, growth of Ha and φ impose a negative impact on the magnitude of Nu_{avg}, which is depicted in Fig. 19(a)–(c). But at $Ha = 40$, φ causes an increment in Nu_{avg} profile.

To figure out the influences of rotation angle of inner cylinder (ω) on Nu_{avg} against φ has been depicted in Fig. 20(a)–(c). The outcome reveals that, Nu_{avg} is gradually decreasing for increasing n. That means, heat transfer is fast and the strength of the fluid flow is stronger when the viscous effects are low ($n < 1$). Moreover, the greater values of solid volumetric concentration of nanoparticles are weaken heat transfer rate. The value $\varphi = 0.04$ makes a considerable reduction on Nu_{avg} at $n = 0.8$, 1.0 and 1.4. ω shows an irregular control on Nu_{avg} at different phases of non-Newtonian nanofluid.

Figs. 21(a)–(c), 22(a)–(c), 23(a)–(c) and 24(a)–(c), respectively present the distribution of Nu_{avg} along the hot cylinder for distinct values of Ha, Ra, φ and ω with changing the range of γ for non-Newtonian and Newtonian nanofluid. In Fig. 21(a)–(c), as the value of γ at certain Ha rises, it is noticeable that the values of Nu_{avg} are gradually rising as well. Previously, it is described that, the

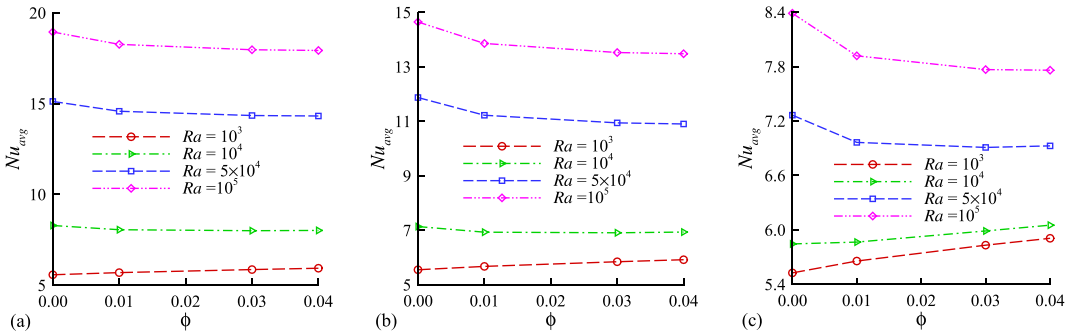

Fig. 18. Nu_{avg} versus solid volume fraction (φ) for several Ra for (a) $n = 0.8$ (b) $n = 1.0$ and (c) $n = 1.4$ at $Ha = 10$, $\gamma = 45^{\circ}$, $\omega = 135^{\circ}$ and Pr = 6.57.

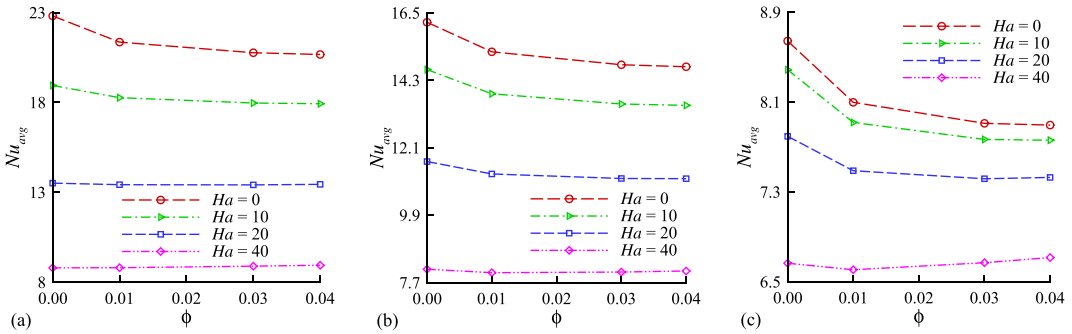

Fig. 19. Nu_{avg} versus solid volume fraction (φ) for several Ha for (a) $n = 0.8$ (b) $n = 1.0$ and (c) $n = 1.4$ at $Ra = 10^5$, $\gamma = 45^{\circ}$, $\omega = 135^{\circ}$ and Pr = 6.57.

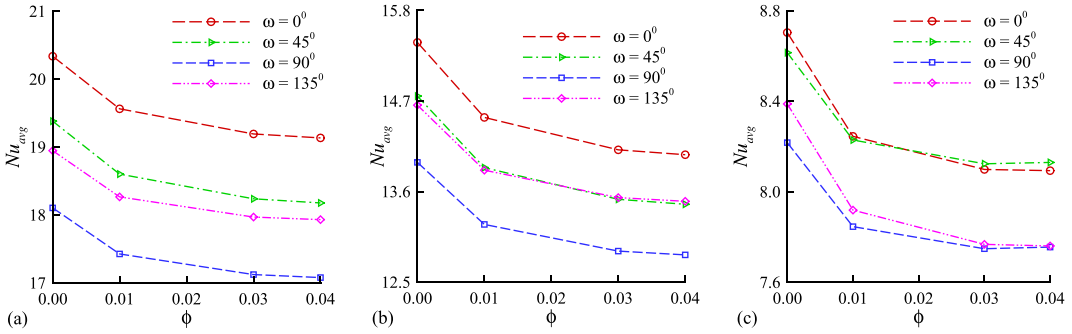

Fig. 20. Nu_{avg} versus rotation angle of inner cylinder (ω) for several φ for (a) $n = 0.8$ (b) $n = 1.0$ and (c) $n = 1.4$ at $Ra = 10^5$, $Ha = 10$, $\gamma = 45^{\circ}$ and Pr = 6.57.

magnetic field becomes more dominant as Ha rises. But the existence of the magnetic field reduces the thermal field and natural convection flow. As a result, Nu_{avg} gradually decreases as Ha rises, whereas an increase in γ accelerates the growth of heat transfer. The results suggest that increasing heat transfer can be done by changing the angle of the magnetic field's orientation toward the top. According to Figs. 21(a)–(c), 22(a)–(c), 23(a)–(c) and 24(a)–(c), Ra, φ and ω produce a slight change in the rate of heat transfer for shear thinning ($n = 0.8$) nanofluid but are less significant for Newtonian ($n = 1.0$) and shear thickening ($n = 1.4$) nanofluid. So, the rate of heat transfer is accelerated when a fluid is shear thinned, whereas Nu_{avg} gradually decreases as a fluid becomes shear thickened.

Figs. 25(a)–(c), 26(a)–(c) and 27(a)–(c) show a comparison between the several models applied for viscosity and thermal conductivity on Nu_{avg} for different stages of Newtonian (26(a)–(c)) and non−Newtonian (25(a)–(c) and 27(a)–(c)) Al_2O_3–water nanofluid (see Fig. 24). These graphs reveal the outcomes obtained from four different combinations of viscosity and thermal conductivity models. As shown in Fig. 25(a)–(c), 26(a)–(c) and 27(a)–(c), it is clear that the difference between the normalized average Nusselt number ($Nu_{avg}(\varphi)/Nu_{avg}(\varphi = 0)$) computed by utilizing the Chon et al. [38] model and the Maxwell [42] model with the Nguyen et al. [40] is relatively small. However, the difference in $Nu_{avg}(\varphi)/Nu_{avg}(\varphi = 0)$ when using Brinkman [41] models is more significant. This indicates that for higher Ra, the effect of thermal conductivity models is less significant than that of viscosity models. For all values of n (n = 0.8, 1.0 and 1.4) and Ra (10^3, 10^4 and 10^5) Chon et al. [38], Maxwell [42] and Nguyen et al. [40] model expose the same

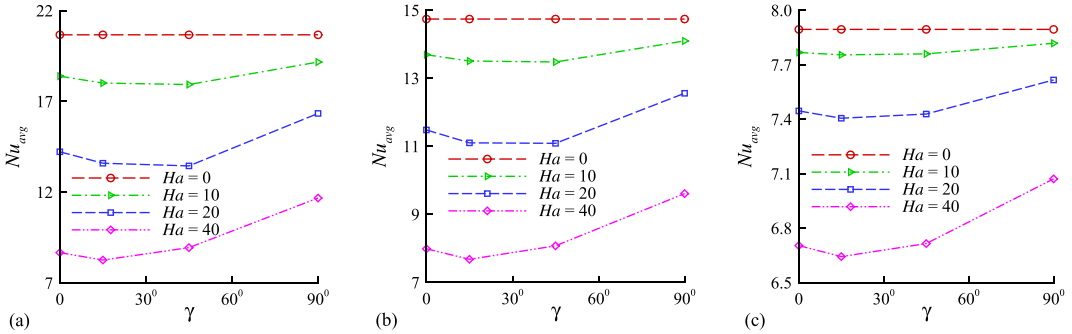

Fig. 21. Nu_{avg} versus magnetic field orientation angle (γ) for several Ha for (a) $n = 0.8$ (b) $n = 1.0$ and (c) $n = 1.4$ at $Ra = 10^5$, $\varphi = 0.04$, $\omega = 135^\circ$ and Pr = 6.57.

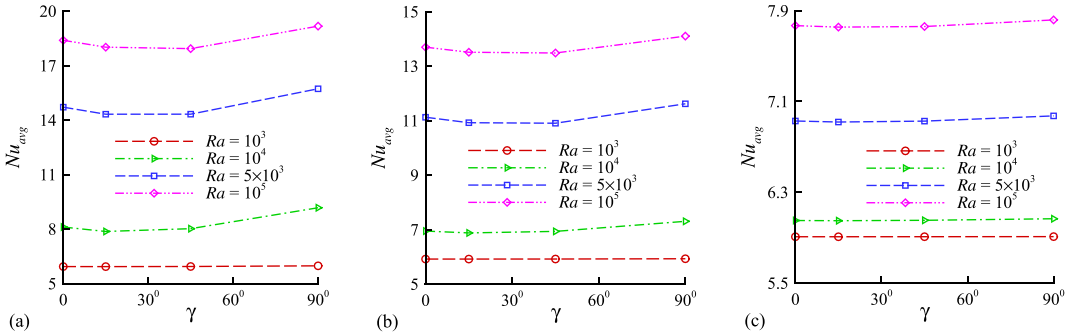

Fig. 22. Nu_{avg} versus magnetic field orientation angle (γ) for several Ra for (a) $n = 0.8$ (b) $n = 1.0$ and (c) $n = 1.4$ at $Ha = 10$, $\varphi = 0.04$, $\omega = 135^\circ$ and Pr = 6.57.

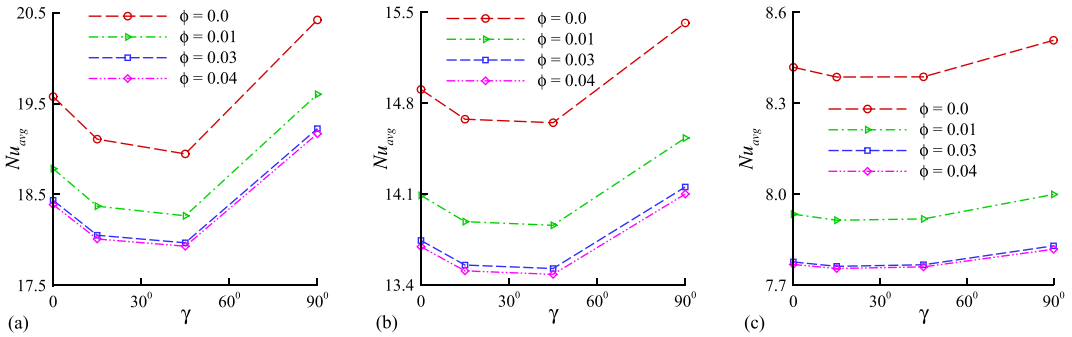

Fig. 23. Nu_{avg} versus magnetic field orientation angle (γ) for several φ for (a) $n = 0.8$ (b) $n = 1.0$ and (c) $n = 1.4$ at $Ra = 10^5$, $Ha = 10$, $\omega = 135^\circ$ and Pr = 6.57.

increasing value. This situation is also true for (Chon et al. [38], Brinkman [41] model) and (Maxwell [42], Brinkman [41] model) combination. For higher Ra ($Ra = 10^5$), $n = 0.8$, 1.0 and 1.4, reduction in heat transfer by using Nguyen et al. [40] data, while heat transfer enhancement can be achieved by employing the Brinkman [41] model. As a result, the calculation of the Nusselt number utilizing Nguyen data appears to diverge from the Brinkman model at $\varphi > 0.0$. The graphical representation of this phenomenon can be observed from Figs. 25(a)–(c), 26(b, c) and 27(c). Also, Figs. 25(b and c), 26(b, c) and 27(b, c) show that the difference between the Chon model and the Maxwell model becomes more noticeable for Ra $> 10^3$, especially at high φ.

7. Conclusions

The natural convective steady and laminar flow of magnetohydrodynamic, non-Newtonian Al_2O_3−water nanofluid in a wavy complex shaped cavity was studied. An inclined elliptic cylinder was considered at the midpoint of the enclosure. Wavy walls were assumed on the right and left parts of the cavity and cooled isothermally. With the aim of providing clear perception, the numerical

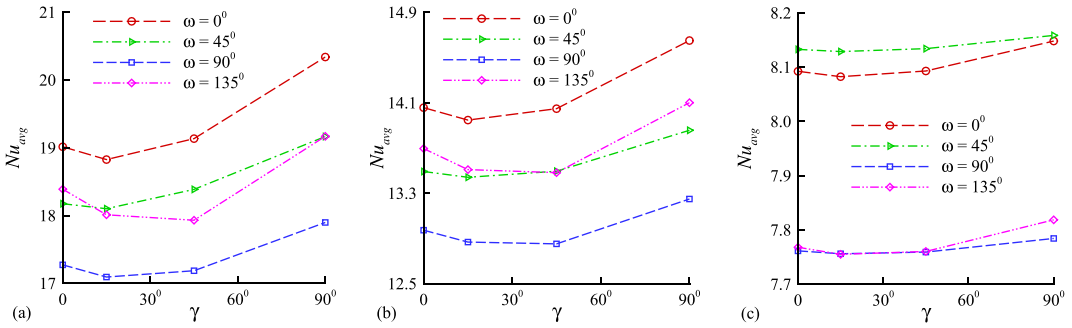

Fig. 24. Nu_{avg} versus magnetic field orientation angle (γ) for several ω for (a) $n = 0.8$ (b) $n = 1.0$ and (c) $n = 1.4$ at $Ra = 10^5$, $Ha = 10$, $\varphi = 0.04$, and $\mathrm{Pr} = 6.57$.

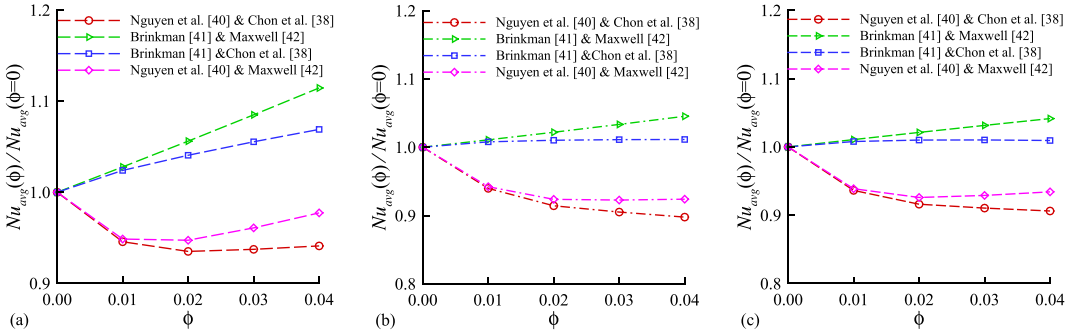

Fig. 25. $Nu_{avg}(\varphi)/Nu_{avg}(\varphi = 0)$ versus φ around the hot inner cylinder for various viscosity and conductivity models for (a) $Ra = 10^3$, (b) $Ra = 10^4$ and (c) $Ra = 10^5$ at $n = 0.8$.

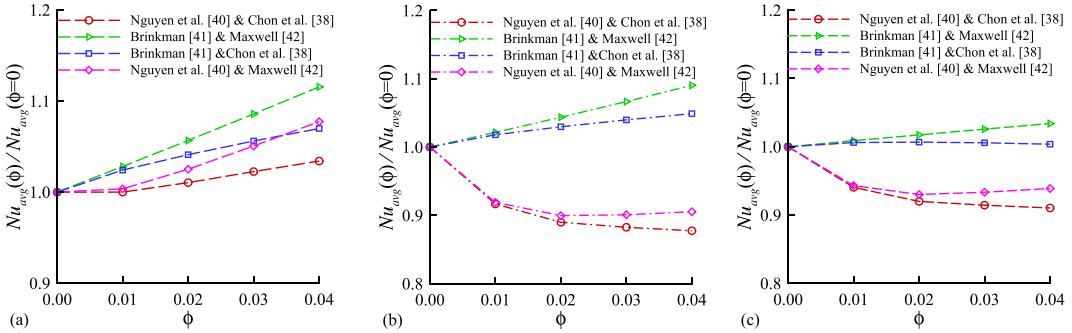

Fig. 26. $Nu_{avg}(\varphi)/Nu_{avg}(\varphi = 0)$ versus φ around the hot inner cylinder for various viscosity and conductivity models for (a) $Ra = 10^3$, (b) $Ra = 10^4$ and (c) $Ra = 10^5$ at $n = 1.0$.

results have been presented via graphical depiction. The most significant findings from this current study are listed below:

(i) Increasing *Ha* causes a reduction in the fluid movement and heat transfer rate. But γ exhibits the opposite tendency. The values of Nu_{avg} are growing gradually for rising the scale of γ at distinct *Ha.* Maximum value is detected for $\gamma = 90^{\circ}$.

(ii) *Ra* shows a directly proportional relationship with the heat transfer rate and flow intensity, which strongly influence the isotherm and stream function distribution mechanisms.

(iii) The reduction in the viscosity of non-Newtonian nanofluid occurs when the power-law index, *n*, becomes smaller. The fluid movement is increased by the shear-thinning fluid ($n < 1$), while the shear-thickening fluid ($n > 1$) starts to slow the flow of the fluid. The fluid flow and heat transfer rate for shear thinning fluid are dominated by thermal convection and for shear thickening fluid by conduction.

(iv) The productivity of the heat transfer rate is slowed down by the addition of Al_2O_3 nanoparticles to the base fluid. Ascending values of *Ra* combined with a higher ratio of the nanoparticles to the base fluid at the shear thinning phase yield a comparatively better thermal performance.

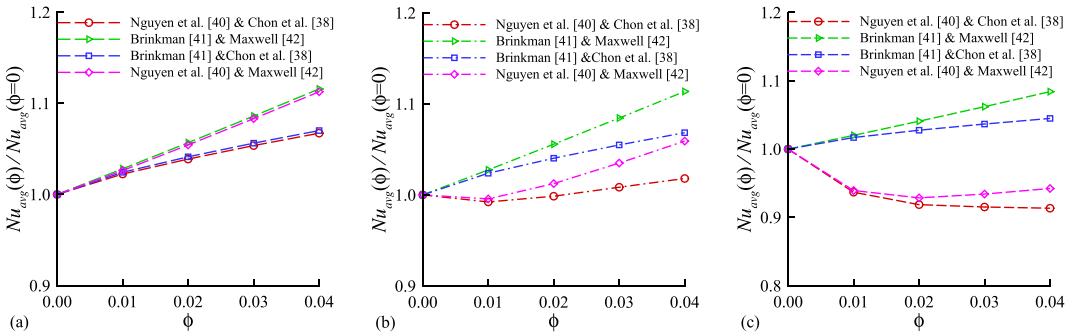

Fig. 27. $Nu_{avg}(\varphi)/Nu_{avg}(\varphi = 0)$ versus φ around the hot inner cylinder for various viscosity and conductivity models for (a) $Ra = 10^3$, (b) $Ra = 10^4$ and (c) $Ra = 10^5$ at $n = 1.4$.

(v) The intensity of convective flow is also affected by the rotation angle of inner cylinder. At $\varphi = 0.04$, both for Newtonian and non-Newtonian fluids, the highest fluid circulation is detected for $\omega = 45^\circ$ and the minimum is found for $\omega = 135^\circ$.

This study's limitations include the fact that the outcomes are accurate under the assumptions of constant thermophysical properties (except viscosity and thermal conductivity), the Boussinesq approximation and thermal equilibrium.

Author contribution statement

Salaika Parvin: Conceived and designed the analysis; Analyzed and interpreted the data; Wrote the paper.
Nepal Chandra Roy, Litan Kumar Saha: Conceived and designed the analysis; Wrote the paper.

Data availability statement

Data will be made available on request.

Declaration of competing interest

The authors declare that they have no known competing financial interests or personal relationships that could have appeared to influence the work reported in this paper.

Acknowledgments

Author (Salaika Parvin) would like to express her sincere appreciation to the Ministry of Science and Technology (MOST), Government of the People's Republic of Bangladesh for providing her research allowance for Ph.D. program.

References

[1] T. Bouhal, S. Fertahi, T. Kousksou, A. Jamil, CFD Thermal energy storage enhancement of PCM filling a cylindrical cavity equipped with submerged heating sources, J. Energy Storage 18 (2018) 360–370, https://doi.org/10.1016/j.est.2018.05.015.
[2] S. Xie, H. Wang, Q. Wu, Y. Liu, Y. Zhang, J. jin, C. Pei, A study on the thermal performance of solar oven based on phase-change heat storage, Energy Explor. Exploit. 37 (5) (2019) 1487–1501, https://doi.org/10.1177/0144598718795491.
[3] A. Yatağanbaba, I. Kurtbaş, Effect of heating position on thermal energy storage in cavity with/without open-cell metallic foams, Exp. Heat Tran. 29 (3) (2016) 1–23, https://doi.org/10.1080/08916152.2014.989376.
[4] L. Li, Z. Tang, H. Li, W. Gao, Z. Yue, G. Xie, Convective heat transfer characteristics of twin-web turbine disk with pin fins in the inner cavity, Int. J. Therm. Sci. 152 (6) (2020), 106303, https://doi.org/10.1016/j.ijthermalsci.2020.106303.
[5] Y. Liu, S. Zhang, H. Huang, Q. Suo, Y. Bian, Y. Zhao, Enhancing the flow and heat transfer in a convective cavity using symmetrical and adiabatic twin fins, Int. J. Heat Mass Tran. 142 (10) (2019), 118447, https://doi.org/10.1016/j.ijheatmasstransfer.2019.118447.
[6] M. Arıcı, E. Tütüncü, Ç. Yıldız, D. Li, Enhancement of PCM melting rate via internal fin and nanoparticles, Int. J. Heat Mass Tran. 156 (2020), 119845, https://doi.org/10.1016/j.ijheatmasstransfer.2020.119845.
[7] F. Selimefendigil, H.F. Oztop, Control of natural convection in a CNT-water nanofluid filled 3D cavity by using an inner T-shaped obstacle and thermoelectric cooler, Int. J. Mech. Sci. 169 (2020), 105104, https://doi.org/10.1016/j.ijmecsci.2019.105104.
[8] N.S. Gibanov, M.A. Sheremet, I. Pop, Natural convection of micropolar fluid in a wavy differentially heated cavity, J. Mol. Liq. 221 (2016) 518–525, https://doi.org/10.1016/j.molliq.2016.06.033.
[9] E.B. Öğüt, M. Akyol, M. Arici, Natural convection of nanofluids in an inclined square cavity with side wavy walls, J. Therm. Sci. Technol. 37 (2) (2017) 139–150.
[10] M. Arici, M. Kan, H. Karabay, Effect of aspect ratio on natural convection in a cavity with wavy walls, Acta Phys. Pol., A 128 (2) (2015) 197–200, https://doi.org/10.12693/APhysPolA.128.B-197.
[11] M. Yuan, R. Mohebbi, M.M. Rashidi, Y. Zhigang, Simulation of nanofluid natural convection in a U-shaped cavity equipped by a heating obstacle: effect of cavity's aspect ratio, J. Taiwan Inst. Chem. Eng. 93 (2018) 263–276, https://doi.org/10.1016/j.jtice.2018.07.026.
[12] P. Chorin, F. Moreau, D. Saury, Heat transfer modification of a natural convection flow in a differentially heated cavity by means of a localized obstacle, Int. J. Therm. Sci. 151 (2020), 106279, https://doi.org/10.1016/j.ijthermalsci.2020.106279.

[13] C. Qi, J. Tang, Z. Ding, Y. Yan, L. Guo, Y. Ma, Effects of rotation angle and metal foam on natural convection of nanofluids in a cavity under an adjustable magnetic field, Int. Commun. Heat Mass Tran. 109 (2019), 104349, https://doi.org/10.1016/j.icheatmasstransfer.2019.104349.

[14] C.C. Cho, Mixed convection heat transfer and entropy generation of Cu−water nanofluid in wavy−wall lid-driven cavity in presence of inclined magnetic field, Int. J. Mech. Sci. 151 (2) (2019) 703–714, https://doi.org/10.1016/j.ijmecsci.2018.12.017.

[15] F. Selimefendigil, H.F. Oztop, Effects of conductive curved partition and magnetic field on natural convection and entropy generation in an inclined cavity filled with nanofluid, Phys. Stat. Mech. Appl. 540 (2020), 123004, https://doi.org/10.1016/j.physa.2019.123004.

[16] M.H. Matin, W.A. Khan, Laminar natural convection of non-Newtonian power law fluids between concentric circular cylinders, Int. Commun. Heat Mass Tran. 43 (2013) 112–121, https://doi.org/10.1016/j.icheatmasstransfer.2013.02.006.

[17] K. Khellaf, G. Lauriat, Numerical study of heat transfer in a non-Newtonian Carreau-fluid between rotating concentric vertical cylinders, J. Non-Newtonian Fluid Mech. 89 (1–2) (2000) 45–61, https://doi.org/10.1016/S0377-0257(99)00030-0.

[18] J.A. Esfahani, V. Bordbar, Double diffusive natural convection heat transfer enhancement in a square enclosure using nanofluids, J. Nanotechnol. Eng. Med. 2 (2) (2011), 021002, https://doi.org/10.1115/1.4003794.

[19] H. Ozoe, S.W. Churchill, Hydrodynamic Stability and Natural Convection in Ostwald–De Waele and Ellis Fluids: the Development of Numerical Solution, vol. 18, American Institute of Chemical Engineers, 1972, pp. 1196–1207, https://doi.org/10.1002/aic.690180617.

[20] D. Li, H. Zhang, P. Ye, Z. Yu, Natural convection of power-law nanofluid in a square enclosure with a circular cylinder: an immersed boundary-lattice Boltzmann study, Int. J. Mod. Phys. C 29 (11) (2018) 1–13, https://doi.org/10.1142/S012918311850105X.

[21] A. Jahanbakhshi, A.A. Nadooshan, M. Bayareh, Magnetic field effects on natural convection flow of a non-Newtonian fluid in an L-shaped enclosure, J. Therm. Analy. Calor. 133 (2018) 1407–1416, https://doi.org/10.1007/s10973-018-7219-6.

[22] F.H. Ali, H.K. Hamzah, K. Egab, M. Arıcı, A. Shahsavar, Non-Newtonian nanofluid natural convection in a U-shaped cavity under magnetic field, Int. J. Mech. Sci. 186 (2020), 105887, https://doi.org/10.1016/j.ijmecsci.2020.105887.

[23] Q. Sun, I. Pop, Free convection in a triangle cavity filled with a porous medium saturated with nanofluids with flush mounted heater on the wall, Int. J. Therm. Sci. 50 (2011) 2141–2153, https://doi.org/10.1016/j.ijthermalsci.2011.06.005.

[24] N. Makulati, A. Kasaeipoor, M.M. Rashidi, Numerical study of natural convection of a water-alumina nanofluid in inclined C-shaped enclosures under the effect of magnetic field, Adv. Powder Technol. 27 (2) (2016) 661–672, https://doi.org/10.1016/j.apt.2016.02.020.

[25] Y. Menni, A.J. Chamkha, C. Zidani, B. Benyoucef, Baffle orientation and geometry effects on turbulent heat transfer of a constant property incompressible fluid flow inside a rectangular channel, Int. J. Numer. Methods Heat Fluid Flow 30 (6) (2019) 3027–3052, https://doi.org/10.1108/HFF-12-2018-0718.

[26] S.E. Ahmed, M.A. Mansour, A.M. Rashad, T. Salah, MHD natural convection from two heating modes in fined triangular enclosures filled with porous media using nanofluids, J. Therm. Analy. Calor. 139 (2020) 3133–3149, https://doi.org/10.1007/s10973-019-08675-x.

[27] M. Hirpho, W. Ibrahim, Dynamics of flow in trapezoidal enclosure having a heated inner circular cylinder containing Casson nanofluid, Heliyon 7 (7) (2021), e07683, https://doi.org/10.1016/j.heliyon.2021.e07683.

[28] A. Abdulkadhim, H.K. Hamzah, F.H. Ali, A.M. Abed, I.M. Abed, Natural convection among inner corrugated cylinders inside wavy enclosure filled with nanofluid superposed in porous–nanofluid layers, Int. Commun. Heat Mass Tran. 109 (2019), 104350, https://doi.org/10.1016/j.icheatmasstransfer.2019.104350.

[29] A.K. Hussein, H.K. Hamzah, F.H. Ali, L. Kolsi, Mixed convection in a trapezoidal enclosure filled with two layers of nanofluid and porous media with a rotating circular cylinder and a sinusoidal bottom wall, J. Therm. Analy. Calor. 141 (2020) 2061–2079, https://doi.org/10.1007/s10973-019-08963-6.

[30] S.U.S. Choi, J.A. Eastman, Enhancing Thermal Conductivity of Fluids with Nanoparticles, ASME International mechanical engineering congress and exhibition, United States, 1995, p. 231.

[31] M. Mahmoodi, S.M. Hashemi, Numerical study of natural convection of a nanofluid in C-shaped enclosures, Int. J. Therm. Sci. 55 (2012) 76–89, https://doi.org/10.1016/j.ijthermalsci.2012.01.002.

[32] M.K. Koopaee1, A. Omidvar, I. Jelodari, Numerical study on the steady-state heat transfer rate of nanofluid filled within square cavity in the presence of oriented magnetic field, Proc. IME C J. Mech. Eng. Sci. 228 (8) (2014) 1348–1362, https://doi.org/10.1177/0954406213507.

[33] I.M. Abed, A. Abdulkadhim, R.A. Hamzah, H.K. Hammed, F.H. Ali, Natural convection heat transfer for adiabatic circular cylinder inside trapezoidal enclosure filled with a nanofluid superposed porous–nanofluid layer, FME Trans. 48 (2020) 82–89, https://doi.org/10.5937/fmet2001082M.

[34] S. Mojumder, K.M. Rabbi, S. Saha, M.N. Hasan, S.C. Saha, Magnetic field effect on natural convection and entropy generation in a halfmoon shaped cavity with semi-circular bottom heater having different ferrofluid inside, J. Magn. Magn Mater. 407 (2016) 412–424, https://doi.org/10.1016/j.jmmm.2016.01.046.

[35] F. Selimefendigil, H.F. Öztop, Conjugate natural convection in a nanofluid filled partitioned horizontal annulus formed by two isothermal cylinder surfaces under magnetic field, Int. J. Heat Mass Tran. 108 (2017) 156–171, https://doi.org/10.1016/j.ijheatmasstransfer.2016.11.080.

[36] M. Sheikholeslami, S.A. Shehzad, Non-Darcy free convection of Fe_3O_4−water nanoliquid in a complex shaped enclosure under impact of uniform Lorentz force, Chin. J. Phys. 56 (2018) 270–281, https://doi.org/10.1016/j.cjph.2017.12.017.

[37] A.M. Rashad, M.M. Rashidi, G. Lorenzini, S.E. Ahmed, A.M. Aly, Magnetic field and internal heat generation effects on the free convection in a rectangular cavity filled with a porous medium saturated with Cu−water nanofluid, Int. J. Heat Mass Tran. 104 (2017) 878–889, https://doi.org/10.1016/j.ijheatmasstransfer.2016.08.025.

[38] C.H. Chon, K.D. Kihm, S.P. Lee, S.U.S. Choi, Empirical correlation finding the role of temperature and particle size for nanofluid (Al_2O_3) thermal conductivity enhancement, Appl. Phys. Lett. 87 (15) (2005), 153107, https://doi.org/10.1063/1.2093936.

[39] E. Abu-Nada, Effects of variable viscosity and thermal conductivity of Al_2O_3–water nanofluid on heat transfer enhancement in natural convection, Int. J. Heat Fluid Flow 30 (2009) 679–690, https://doi.org/10.1016/j.ijheatfluidflow.2009.02.003.

[40] C.T. Nguyen, F. Desgranges, G. Roy, N. Galanis, T. Mare, S. Boucher, H. Angue Minsta, Temperature and particle-size dependent viscosity data for water-based nanofluids–Hysteresis phenomenon, Int. J. Heat Fluid Flow 28 (6) (2007) 1492–1506, https://doi.org/10.1016/j.ijheatfluidflow.2007.02.004.

[41] H.C. Brinkman, The viscosity of concentrated suspensions and solution, J. Chem. Phys. 20 (4) (1952) 571–581, https://doi.org/10.1063/1.1700493.

[42] J.C. Maxwell-Garnett, Colours in metal glasses and in metallic films, Philos. Trans. R. Soc. London, Ser. A 203 (1904) 385–420, https://doi.org/10.1098/rsta.1904.0024.

[43] O. Turan, A. Sachdeva, N. Chakraborty, R.J. Poole, Laminar natural convection of power-law fluids in a square enclosure with differentially heated side walls subjected to constant temperatures, J. Non-Newtonian Fluid Mech. 166 (17–18) (2011) 1049–1063, https://doi.org/10.1016/j.jnnfm.2011.06.003.

[44] B. Ghasemi, S.M. Aminossadati, A. Raisi, Magnetic field effect on natural convection in a nanofluid-filled square enclosure, Int. J. Therm. Sci. 50 (9) (2011) 1748–1756, https://doi.org/10.1016/j.ijthermalsci.2011.04.010.

[45] G. Cesini, M. Paroncini, G. Cortella, M. Manzan, Natural convection from a horizontal cylinder in a rectangular cavity, Int. J. Heat Mass Tran. 42 (10) (1999) 1801–1811, https://doi.org/10.1016/S0017-9310(98)00266-X.

[46] S. Hussain, T. Tayebi, T. Armaghani, A.M. Rashad, H.A. Nabwey, Conjugate natural convection of non-Newtonian hybrid nanofluid in wavy-shaped enclosure, Appl. Math. Mech. 43 (3) (2022) 447–466, https://doi.org/10.1007/s10483-022-2837-6.

[47] T. Tayebi, H.F. Öztop, A.J. Chamkha, MHD natural convection of a CNT-based nanofluid-filled annular circular enclosure with inner heat-generating solid cylinder, Eur. Phy. J. Plus 136 (2021) 150, https://doi.org/10.1140/epjp/s13360-021-01106-7.